Cell Reports
Medicine

Article

Impact of the tumor immune contexture in microsatellite-stable metastatic colorectal cancer treated with avelumab, cetuximab, and irinotecan

Graphical abstract

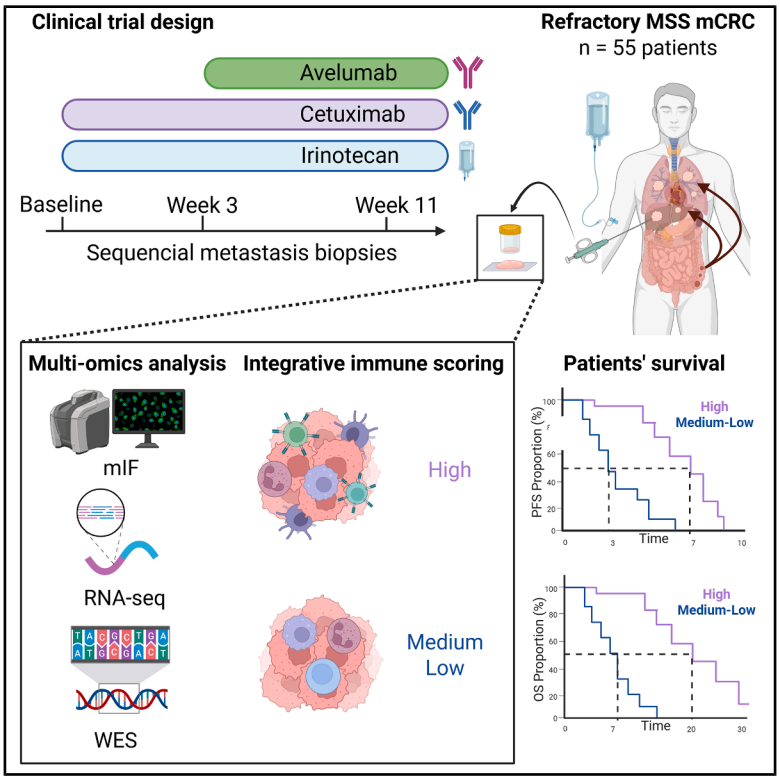

Highlights

- The study treatment showed manageable safety and some efficacy
- Baseline immune contexture strongly stratified patient survival
- Integrative mIF, RNA-seq, and WES uncovered immune-related biomarkers
- Identified biomarkers could guide ICI use in MSS mCRC

Authors

Nicolas Huyghe, Elena Benidovskaya, Tariq Masoodi, ..., Wouter R.L. Hendrickx, Javier Carrasco, Marc Van den Eynde

Correspondence

whendrickx@sidra.org (W.R.L.H.), marc.vandeneynde@uclouvain.be (M.V. d.E.)

In brief

Huyghe et al. report that patients with refractory microsatellite-stable metastatic colorectal cancer benefit from avelumab-based therapy when their tumors have a pre-existing immunogenic microenvironment. Biomarkers such as biopsy-adapted Immunoscore, T cell proximity to tumor cells, and immunoediting score in metastases are associated with improved survival outcomes.

Huyghe et al., 2025, Cell Reports Medicine 6, 102201
July 15, 2025
https://doi.org/10.1016/j.xcrm.2025.102201

CellPress

Cell Reports Medicine

CellPress
OPEN ACCESS

Article

Impact of the tumor immune contexture in microsatellite-stable metastatic colorectal cancer treated with avelumab, cetuximab, and irinotecan

Nicolas Huyghe,[1] Elena Benidovskaya,[1] Tariq Masoodi,[2] Isabelle Sinapi,[3] Astrid De Cuyper,[4,5] Fazulur Vempalli,[2] Simon Beyaert,[1] Caroline Bouzin,[11] Finoula Maestre Osorio,[1] Luigi Ferraro,[10] Nicolas van Baren,[9] Raphaël Helaers,[9] Pierre Goffette,[5,6] Benoit Ghaye,[5,7] Aline van Maanen,[5] Marie-Laure Castella,[5] Michele Ceccarelli,[10] Davide Bedognetti,[2] Jérôme Galon,[8] Wouter R.L. Hendrickx,[2,13,*] Javier Carrasco,[3] and Marc Van den Eynde[1,4,5,12,14,*]

[1]IREC MIRO-ONCO, Laboratory of Oncology, UCLouvain, Brussels, Belgium
[2]Tumor Biology and Immunology Lab, Research Branch, Sidra Medicine, Al-Rayyan, Qatar
[3]Medical Oncology Department, Grand Hopital de Charleroi - Site Notre Dame, Charleroi, Belgium
[4]Medical Oncology Department, Cliniques Universitaires Saint-Luc, Brussels, Belgium
[5]Institut Roi Albert II, Cliniques Universitaires Saint-Luc, Brussels, Belgium
[6]Unité de Radiologie Interventionnelle, Cliniques Universitaires Saint-Luc, Brussels, Belgium
[7]Service d'Imagerie Interventionnelle, Cliniques Universitaires Saint-Luc, Brussels, Belgium
[8]INSERM, Laboratory of Integrative Cancer Immunology, Centre de Recherche des Cordeliers, Université Paris Cité, Sorbonne Université, Paris, France
[9]de Duve Institute - UCLouvain, Av. Hippocrate 75, 1200 Woluwe-Saint-Lambert, Belgium
[10]Department of Public Health Sciences, Sylvester Comprehensive Cancer Center Miller School of Medicine, University of Miami, 1550 NW 10th Avenue, Miami, FL 33136, USA
[11]IREC Imaging Platform (2IP - RRID:SCR_023378), Université Catholique de Louvain, Brussels, Belgium
[12]Gastroenterology Department, Cliniques Universitaires Saint-Luc, Brussels, Belgium
[13]College of Health and Life Sciences (CHLS), Hamad bin Khalifa University (HBKU), Doha, Qatar
[14]Lead contact
*Correspondence: whendrickx@sidra.org (W.R.L.H.), marc.vandeneynde@uclouvain.be (M.V.d.E.)
https://doi.org/10.1016/j.xcrm.2025.102201

SUMMARY

The treatment of patients with microsatellite-stable (MSS) metastatic colorectal cancer (mCRC) remains a significant clinical challenge. Cetuximab, an anti-epidermal growth factor receptor (EGFR) monoclonal antibody (mAb), induces immunogenic cell death, potentially synergizing with immune checkpoint inhibitors. The phase 2, proof-of-concept, single-arm AVETUXIRI trial (ClinicalTrials.gov: NCT03608046) evaluates the safety and efficacy of cetuximab, irinotecan (a topoisomerase I inhibitor), and avelumab (an anti-programmed cell death ligand 1 [PD-L1]) in 57 patients with *RAS* wild-type or mutated MSS mCRC refractory to chemotherapy and anti-EGFR mAbs. Exploratory objectives include investigating the tumor immune microenvironment within mCRC biopsies performed during the trial and correlating it with treatment activity. A manageable safety profile is observed. Although the overall efficacy endpoints are not met, biomarkers associated with clinical efficacy are identified. Patients exhibiting a high Immunoscore, strong cytotoxic and T cell proximity to tumor cells, and a high genetic immunoediting score within mCRC biopsies before treatment demonstrate significant therapeutic survival benefit, independent of *RAS* tumor mutation status.

INTRODUCTION

Colorectal cancer (CRC) is the third most diagnosed cancer and the second leading cause of cancer-related deaths worldwide, accounting for approximately 9.3% of all cancer-related deaths each year.[1]

Chemotherapy combined with monoclonal antibody (mAb)-targeting vascular endothelial growth factors (VEGFs) or epidermal growth factor receptors (EGFRs) remains the cornerstone of treatment for metastatic CRC (mCRC).[2,3] Testing for deficient mismatch repair (dMMR)/microsatellite instability-high (MSI-H) status, as well as *RAS* (including *KRAS* and *NRAS* exons 2, 3, and 4) and *BRAF* mutations, is recommended due to its relevance for patient prognosis and the selection of systemic therapy.[2,3] *RAS* mutations, which activate the EGFR pathway downstream of the receptor, along with right-sided primary tumor location, are recognized as negative predictive factors for the use of anti-EGFR mAbs.[4,5]

Immune checkpoint inhibitors (ICIs) targeting programmed cell death (ligand) 1 (PD-[L]1) and cytotoxic T lymphocyte-associated protein 4 (CTLA-4) demonstrate remarkable efficacy in dMMR/MSI-H CRC,[6–9] likely due to an increased neoantigen

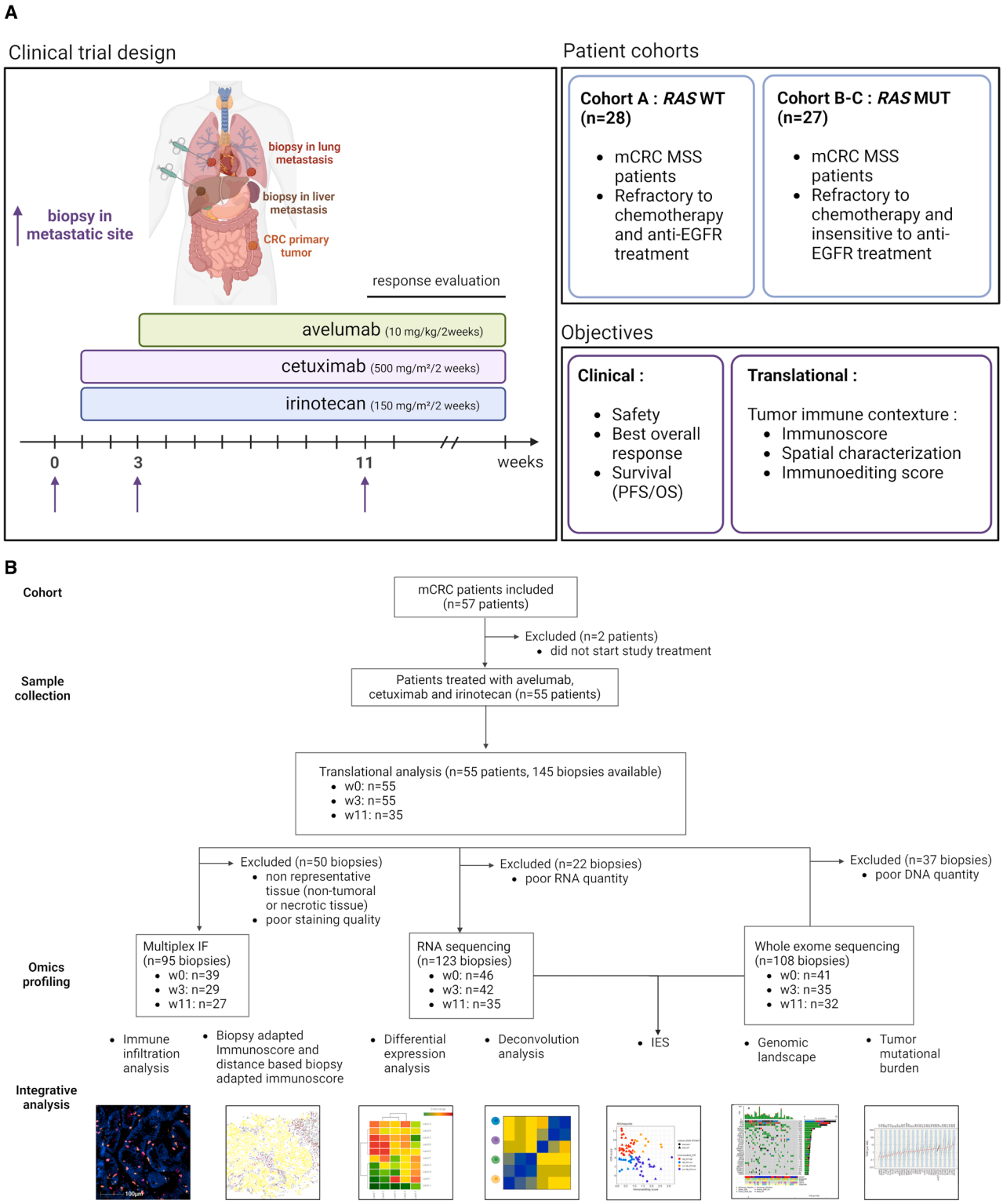

Figure 1. Clinical trial design, patient cohorts, and omics profiling workflow

(A) Clinical trial design and patient cohorts. Diagram illustrating the study treatment regimen. Treatment with cetuximab (500 mg/m^2 every 2 weeks) and irinotecan (150 mg/m^2 every 2 weeks) started 2 weeks prior to the initiation of avelumab (10 mg/kg every 2 weeks). This combined treatment continued until progression, with the first radiological evaluation at week 11. Metastasis biopsies were collected at baseline (week 0), before avelumab initiation (week 3), and at the first

(legend continued on next page)

load.[10,11] The clinical benefits of ICIs remain elusive for most patients with mismatch repair-proficient or microsatellite-stable (MSS) mCRC lacking pathogenic DNA polymerase epsilon (*POLE*) or delta (*POLD1*) catalytic subunit mutations.[12–15] Biomarkers for selecting immunogenic MSS mCRC potentially responsive to ICIs are under intense investigation. Beyond tumor mutational burden (TMB), recent post hoc analyses from trials suggest that a tumor immune scoring system, named Immunoscore-Immune-Checkpoint (Immunoscore-IC), which quantifies densities of PD-L1$^+$ and CD8$^+$ cells and measures the proximity between CD8$^+$ and PD-L1$^+$ cells within the tumor microenvironment, could serve as a potent biomarker for response to PD-1/PD-L1 ICIs.[16,17]

New strategies are being developed to overcome immune resistance and elicit effective immune responses against tumor cells.[18–21] Cetuximab, a chimeric anti-EGFR mAb, may activate the immune system by inducing innate effector functions through the binding of its Fc region to natural killer (NK) cells.[22] Furthermore, when combined with chemotherapy (including irinotecan), cetuximab induces immunogenic cell death in CRC, independent of *RAS* mutation status, and leads to an increase in tumor-infiltrating CD8$^+$ T cells and NK cells,[23,24] which should synergize with the immunostimulatory effects of ICIs.[25]

Building upon these insights, we initiated the AVETUXIRI trial (ClinicalTrials.gov: NCT03608046), a proof-of-concept, open-label, non-randomized, phase 2a study for patients with chemorefractory, MSS mCRC. The treatment regimen, including cetuximab, irinotecan, and avelumab (an anti-PD-L1 mAb), was evaluated in several patient cohorts, was refractory to anti-EGFR mAbs (acquired resistance for *RAS* wild-type [WT] tumors), and was stratified by *RAS* tumor mutation status. The primary objectives were to assess the efficacy and safety of this combination. Exploratory objectives included an in-depth investigation of the immunological characteristics of the tumor and its surrounding microenvironment, conducted before and during treatment, to identify predictive biomarkers of efficacy.

RESULTS

Patients' characteristics

From October 2018 to June 2022, 57 patients with MSS, chemorefractory mCRC were prospectively enrolled across three distinct cohorts. Cohort A included patients with *RAS* WT tumors (*RAS* WT), while cohorts B and C sequentially enrolled patients with *RAS* mutant tumors (*RAS* MUT). The primary clinical objectives were safety and treatment efficacy. Of these 57 patients, 55 initiated the treatment (Figure 1A).

Patient and tumor characteristics are summarized in Table S1. The median age was 63 years (range: 37–76), with a predominance of male patients (n = 41; 75.5%). The majority of the patients had left-sided (left and rectum) primary tumors (n = 47; 85.5%), underwent primary tumor resection (n = 36; 65.4%), presented with synchronous metastases (n = 48; 87.2%) and liver metastases (n = 49; 89.1%), had metastatic involvement of at least two organs (n = 43; 78.2%), and had received three or more prior lines of therapy (n = 40; 72.7%).

Feasibility and safety

Treatment-emergent adverse events (TEAEs) occurred in all 55 (100%) patients (Table S2). TEAEs grade ≥3 occurred in 35 (63.6%) patients, with irinotecan-related diarrhea being the most frequent (20.0%) (Tables S2 and S3). Immune-related TEAEs occurred in 12 (21.8%) patients (Table S4). Among them, 2 (3.6%) were of a grade ≥3 (acute kidney injury and hepatobiliary injury). TEAEs leading to discontinuation of avelumab, cetuximab, and irinotecan occurred in 3 (5.5%), 1 (1.8%), and 3 (5.5%) patients, respectively (Table S5). No TEAEs leading to death occurred.

Efficacy analyses

Study design and per-protocol efficacy analyses for the different cohorts are summarized in Figure S1 and Table S6. The median follow-up was 9.27 months (95% confidence interval [CI]: 7.96–12.70 months). Among the 28 patients with *RAS* WT mCRC in cohort A, 6 (21.4%) achieved a partial response (PR), 8 (28.6%) had stable disease (SD), and 14 (50.0%) had progressive disease (PD), resulting in a disease control rate (DCR) of 50.0% (PR + SD). The median duration of response was 4.14 months (95% CI: 1.94–4.70 months). In contrast, among the 27 patients with *RAS* MUT mCRC in cohorts B and C, none (0.0%) achieved PR, 14 (51.9%) had SD, and 13 (48.1%) had PD, yielding a DCR of 51.9%. The best overall response (BOR) and duration of response for all included patients are summarized in Figures 2A, 2C, and S1A–S1C.

The median progression-free survival (PFS) was 3.65 months (95% CI: 2.56–5.88 months) for patients with *RAS* WT mCRC and 3.35 months (95% CI: 2.76–4.93 months) for patients with *RAS* MUT mCRC. The 6-month PFS rate was 30.8% (95% CI: 17.4–54.3%) for *RAS* WT, 18.5% (95% CI: 8.4–40.9%) for *RAS* MUT, and 24.6% (95% CI: 15.4–39.3%) for the entire patient population (Figure 2D; Table S6). The median overall survival (OS) was 10.82 months (95% CI: 5.26–13.38 months) for patients

radiological evaluation (week 11). Patients were split into three cohorts (cohort A: *RAS* WT and cohorts B and C: *RAS* MUT), with safety, efficacy, and survival (progression-free survival [PFS] and overall survival [OS]) as clinical objectives. Translational objectives included extensive tumor immune microenvironment analysis and its correlation with clinical efficacy results.

(B) Omics profiling and integrative analysis workflow. Flowchart depicting sample collection, omics profiling, and analysis pipeline. Out of 57 mCRC patients assessed, 55 initiated treatment and contributed a total of 145 biopsies at weeks 0, 3, and 11. Multiplex immunofluorescence (mIF) enabled spatial characterization of the immune microenvironment, utilizing biopsy-adapted (ISb) and distance-based biopsy-adapted (ISb_20) Immunoscores as well as immune cell profiling. RNA-seq supported differential gene expression analysis, deconvolution analysis for immune cell-type inference within the tumor microenvironment, and immunologic constant of rejection (ICR) score. Whole-exome sequencing (WES) data enabled genomic landscape characterization, including mutational profiling, assessment of tumor mutational burden, neoantigen, and genetic immunoediting (GIE). Integrative analysis synthesized findings from mIF, RNA-seq, and WES to elucidate immune infiltration dynamics, transcriptomic changes, and mutational signatures over the course of treatment and correlated this with treatment response and patient survival.

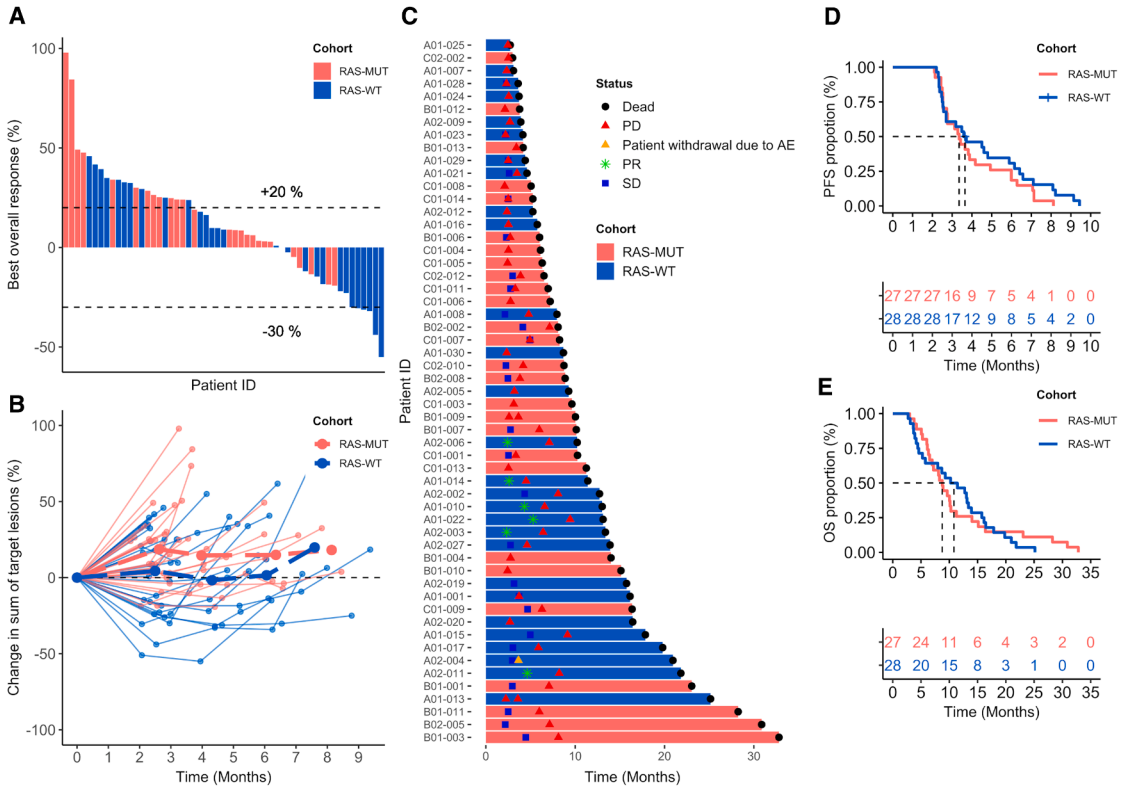

F CoxPH model for OS

Variable		N	Hazard ratio	p
Cohort				
	RAS-MUT	27		
	RAS-WT	28		0.97
Age				
	> 65 years	23		
	≤ 65 years	32		0.09
ECOG status				
	0	28		
	1	27		0.75
LDH levels				
	> 230 U/L	30		
	≤ 230 U/L	25		0.01
Primary tumor location				
	Left	47		
	Right	8		0.32
Primary tumor surgery				
	No	19		
	Yes	36		0.27
Metastases				
	Metachronous	7		
	Synchronous	48		0.23
Liver metastases				
	No	6		
	Yes	49		0.94

G CoxPH model for PFS

Hazard ratio	p
	0.90
	0.64
	0.23
	0.36
	0.08
	0.07
	0.18
	0.17

H Linear model for BOR

Coef.	p
	0.1
	0.6
	0.5
	0.6
	0.1
	0.2
	0.9
	0.1

I CoxPH model for OS (RAS-WT)

Variable		N	Hazard ratio	p
Time from last anti-EGFR treatment				
	> 3 months	9		
	≤ 3 months	19		0.29
Age				
	> 65 years	14		
	≤ 65 years	14		0.24
ECOG status				
	0	11		
	1	17		0.08
LDH levels				
	> 230 U/L	19		
	≤ 230 U/L	9		0.42
Primary tumor location				
	Left	25		
	Right	3		0.74
Primary tumor surgery				
	No	9		
	Yes	19		0.69
Metastases				
	Metachronous	5		
	Synchronous	23		0.04
Liver metastases				
	No	3		
	Yes	25		0.98

J CoxPH model for PFS (RAS-WT)

Hazard ratio	p
	0.198
	0.505
	0.368
	0.233
	0.020
	0.009
	0.194
	0.232

K Linear model for BOR (RAS-WT)

Coef.	p
	0.43
	0.98
	0.41
	0.90
	0.52
	0.03
	0.26
	0.39

(legend on next page)

with *RAS* WT mCRC and 8.75 months (95% CI: 6.97–11.20 months) for patients with *RAS* MUT mCRC. The 12-month OS rate was 46.4% (95% CI: 31.2–69.1%) for *RAS* WT, 25.9% (95% CI: 13.7–49.0%) for *RAS* MUT, and 36.4% (95% CI: 25.6–51.6%) for the entire patient population (Figure 2E; Table S6). The PFS and OS Kaplan-Meier survival curves of cohorts A, B, and C are depicted in Figures S1D and S1E.

Exploratory multivariate analyses of clinical covariates, selected after multiple univariate analyses and stepwise variable selection, were conducted for PFS, OS, and BOR (Figures 2F–2H). A lower lactate dehydrogenase (LDH) level (≤230 U/L) was associated with improved OS (hazard ratio [HR] = 0.40, 95% CI: 0.20–0.81, p = 0.01). Additional multivariate analyses were performed specifically for the *RAS* WT population, incorporating the time from the last anti-EGFR treatment administration before trial inclusion (categorized as over or under 3 months) to investigate a potential "rechallenge" effect of cetuximab (Figures 2I–2K). No associations were observed between the time since the last anti-EGFR treatment and OS, PFS, or BOR. However, synchronous metastases were significantly associated with an elevated risk of mortality (HR = 4.37, 95% CI: 1.10–17.38, p = 0.04). Right-sided primary tumor location was associated with an increased risk of progression (HR = 7.45, 95% CI: 1.37–40.46, p = 0.02), whereas prior surgery of the primary tumor was linked to a reduced risk (HR = 0.22, 95% CI: 0.07–0.69, p = 0.009).

Prespecified efficacy analyses of the study (BOR for cohorts A and B and 6-month PFS rate for cohort C) were not reached (Figure S1; Table S6). Aiming to identify predictive biomarkers of treatment efficacy, the exploratory objectives of the trial, including an in-depth investigation of the immunological characteristics of the tumor and its surrounding microenvironment, are presented thereafter.

Impact of biopsy-adapted Immunoscore on response to treatment and survival

Multiplex immunofluorescence (mIF) staining was performed on 95 metastatic biopsies containing tumor cells and suitable for staining analysis (Figure 1B). Among these, 39 (41%) were analyzed at baseline (prior to the initiation of cetuximab and irinotecan), 29 (30%) at week 3 (before avelumab initiation), and 27 (28%) at week 11 (the first tumor response assessment). Three low-plex panels were developed for staining. The first panel included CD3 (T lymphocytes), CD8 (cytotoxic T lymphocytes), PD-1, PD-L1, and CD45RO (memory lymphocytes). The second panel included CD3, FOXP3 (regulatory T cells and activated T cells), pSMAD3 (marker of transforming growth factor beta [TGF-β] pathway activation), and GAL-9 (β-galactoside lectin protein). The third panel included CD3, Pan-CK (tumor cells), CD68 (monocytes and macrophages), NKp46 (NK cells), and human leukocyte antigen (HLA) class 1 heavy chain (which presents antigens to cytotoxic T cells). Based on CD3 and CD8 T cell densities, a biopsy-adapted Immunoscore (ISb) was derived as described in the "ISb, ISb_20 and heatmap" section of the STAR Methods and according to previously established methodology and to pre-defined cutoffs to categorize patients.[26] Representative scans demonstrating ISb classifications (high, medium, and low) are shown in Figures 3A–3C.

At baseline, 9 patients (23.1%) were classified as ISb high, 20 (51.3%) as ISb medium, and 10 (25.6%) as ISb low (Figure 3D). Median PFS was 7.07 (95% CI: 4.93–not reached), 2.98 (95% CI: 2.70–3.88), and 3.24 (95% CI: 2.37–not reached) months for ISb-high, -medium, and -low groups, respectively (ISb high vs. low: HR = 0.24, 95% CI: 0.09–0.67, $p < 0.007$). No significant difference was observed between the ISb-medium and -low groups. The 6-month PFS rates were 66.7% (95% CI: 42.0%–100.0%) for ISb high, 17.5% (95% CI: 6.4%–47.5%) for ISb medium, and 20.0% (95% CI: 5.8%–69.1%) for ISb low.

Median OS was 13.02 (95% CI: 8.75–not reached), 8.04 (95% CI: 6.02–15.10), and 7.47 (95% CI: 4.06–not reached) months for ISb-high, -medium, and -low groups, respectively (ISb high vs. low: HR = 0.44, 95% CI: 0.17–1.13, p = 0.09) (Figure 3E). The 12-month OS rates were 66.7% (95% CI: 42.0%–100.0%) for ISb high, 30.0% (95% CI: 15.4%–58.6%) for ISb medium, and 20.0% (95% CI: 5.8%–69.1%) for ISb low.

No significant changes in ISb proportions were observed at different treatment time points. However, a significantly higher proportion of ISb high (all time points) was associated with PFS over 6 months, OS over 12 months, and tumor shrinkage (defined as a radiological decrease of the size of the sum of target lesions between baseline and week 11) (Figures 3F–3I). No differences were observed in relation to *RAS* mutation status.

In multivariate models adjusted for OS, PFS, and BOR, baseline ISb-high status was significantly associated with better OS (HR = 0.16, 95% CI: 0.04–0.54, p = 0.003) and PFS (HR = 0.13, 95% CI: 0.03–0.54, p = 0.005), outperforming all other clinical covariates (Figures 3J and 3K). No associations between ISb and BOR were observed (Figure 3L).

Figure 2. Efficacy analyses of *RAS*-MUT and *RAS*-WT cohorts

(A) Waterfall plot depicting the best overall response (BOR) of target lesions (RECIST1.1) in percentage, by patient ID. Bars indicate individual patient responses, with red for *RAS*-MUT and blue for *RAS*-WT cohorts. The dashed lines represent thresholds for partial response (+20%) and progressive disease (−30%).

(B) Spider plot showing the percentage change in the sum of targeted lesions diameters over time for individual patients in both *RAS*-MUT (red) and *RAS*-WT (blue) cohorts. Dashed lines represent aggregated data for each cohort.

(C) Swimmer plot illustrating the duration of treatment and clinical outcomes for each patient. Each bar represents one patient, with red bars corresponding to the *RAS*-MUT cohort and blue bars to *RAS*-WT. Symbols on the bars indicate patient status (all deceased at analysis): progressive disease (PD), stable disease (SD), partial response (PR), and patient withdrawal due to adverse events (AEs).

(D and E) Kaplan-Meier survival curves for progression-free survival (PFS) and overall survival (OS) comparing *RAS*-MUT (red) and *RAS*-WT (blue) cohorts. Tick marks indicate censored patients, and the number of patients at risk is displayed below the plot. Log rank test p values are displayed.

(F–H) Forest plots from Cox proportional hazards (CoxPH) and linear regression multivariate models showing hazard ratios (HRs and 95% CI), regression coefficients (coef. and 95% CI), and corresponding p values for OS, PFS, and BOR, respectively, across various clinical covariates for the overall cohort.

(I–K) Forest plots depicting CoxPH and linear regression multivariate models specific to the *RAS-WT* cohort for OS, PFS, and BOR, respectively, with HRs (HR and 95% CI) or regression coefficients (coef. and 95% CI) and corresponding p values.

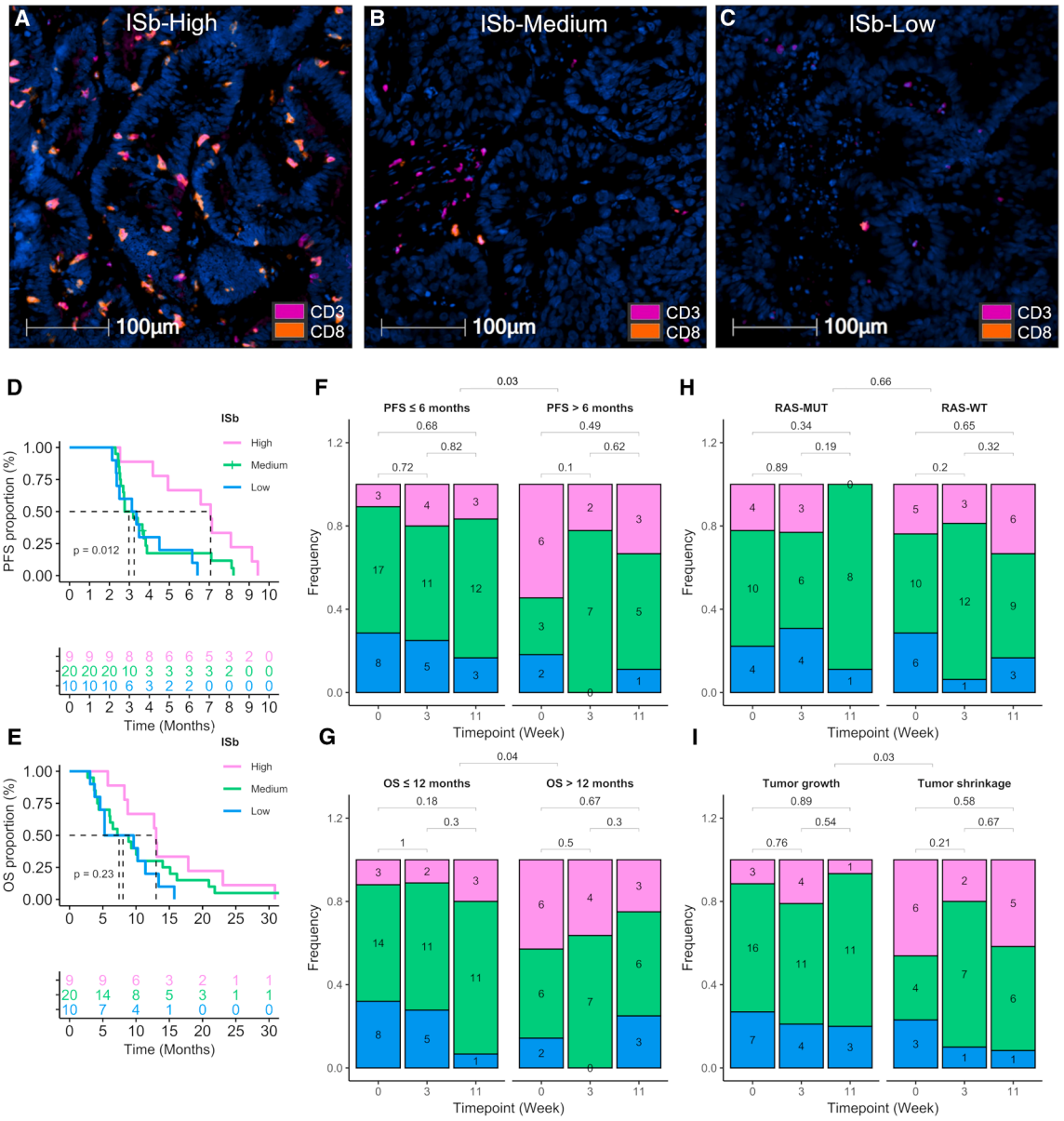

(legend on next page)

Impact of distance-based ISb on patients' response to treatment and survival

Given the unfeasibility of calculating an Immunoscore-IC due to the absence of PD-L1 staining in both mIF and chromogenic staining of metastases biopsies, we developed an alternative, distance-based ISb (ISb_20). Briefly, distances between each $CD8^+$ and $CD3^+$ T cell and tumor cells were calculated, and the G-cross function was employed to assess the probability of each T cell being within a 20-μm range of a tumor cell.[27] These probability data, expressed as the area under the curve (AUC) at 20 μm of the G-cross function, were then used to derive the ISb_20 (Figures 4A–4C).

At baseline, 10 patients (25.6%) were classified as ISb_20 high, 20 (51.3%) as ISb_20 medium, and 9 (23.1%) as ISb_20 low (Figure 4D). Median PFS was 7.07 (95% CI: 4.18–not reached), 3.3 (95% CI: 2.73–4.93), and 2.7 (95% CI: 2.33–not reached) months for ISb_20-high, -medium, and -low groups, respectively (ISb_20 high vs. ISb_20 low: HR = 0.24, 95% CI: 0.09–0.63, p = 0.004). Six-month PFS rates were 67.5% (95% CI: 43.0%–100.0%) for ISb_20 high, 20.0% (95% CI: 8.3%–48.1%) for ISb_20 medium, and 11.1% (95% CI: 1.8%–70.5%) for ISb_20 low.

Median OS was 15.44 (95% CI: 8.88–not reached), 7.73 (95% CI: 6.02–14.0), and 5.26 (95% CI: 3.78–not reached) months for ISb_20-high, -medium, and -low groups, respectively (ISb_20 high vs. ISb_20 low: HR = 0.20, 95% CI: 0.07–0.57, p = 0.003) (Figure 4E). Twelve-month OS rates were 70.0% (95% CI: 46.7%–100.0%) for ISb_20 high, 30.0% (95% CI: 15.4%–58.6%) for ISb_20 medium, and 11.1% (95% CI: 1.8%–70.5%) for ISb_20 low.

Similar to ISb, no significant changes in ISb_20 proportions were observed over time. A significantly higher proportion of ISb_20 high was associated with PFS over 6 months, OS over 12 months, and tumor shrinkage (Figures 4F–4I) but not with RAS tumor mutational status. In paired sample analysis, four patients demonstrated an increase in ISb_20 (corresponding to an increase in $CD3^+$ and $CD8^+$ proximity to tumor cells) between baseline and week 11 (Figure S2A), along with an increase in $CD45RO^+$ and $PD\text{-}1^+$ T cell proximity (as calculated by the G-cross function). Three patients showed a decrease in ISb_20, and 15 patients remained stable. Median PFS was 7.66 (95% CI: 4.18–not reached), 3.65 (95% CI: 2.73–not reached), and 2.55 (95% CI: 2.50–not reached) months for increasing, stable, and decreasing ISb_20, respectively. An increase in ISb_20 was associated with better PFS (p = 0.04) but not with OS (p = 0.71) (Figures S2B and S2C).

In multivariate models adjusted for OS, PFS, and BOR, baseline ISb_20 high was significantly associated with improved OS (ISb_20 high vs. ISb_20 low: HR = 0.09, 95% CI: 0.02–0.34, $p < 0.001$) and PFS (ISb_20 high vs. ISb_20 low: HR = 0.17, 95% CI: 0.05–0.50, p = 0.003), outperforming other clinical covariates (Figures 4J and 4K). No association was observed between ISb_20 and BOR (Figure 4L).

Extensive analysis of the tumor immune microenvironment helps to discriminate patient outcomes

To enrich our analysis of the immune microenvironment, we integrated data on cell densities and distances to tumor cells from the three mIF panels, which included various immune cell staining, into heatmaps. At baseline, unsupervised clustering analysis identified two distinct patient clusters (Figure 5A). The first cluster (light blue) was characterized by high tumor immune scores (ISb and ISb_20) and substantial T cell infiltration, including $CD3^+$ T cells, cytotoxic T cells ($CD3^+CD8^+$), T helper cells ($CD3^+CD8^-$), $PD\text{-}1^+$ cells, and $PD\text{-}1^+$ T cells (both $CD3^+$ and $CD8^+$). In this cluster, four patients had high densities of $CD45RO^+$ T cells ($CD3^+$ and $CD8^+$), indicating memory T cells within the biopsies.

Within this immunogenic cluster, three patients showed close proximity between tumor cells and $CD3^+PD\text{-}1^+$ T cells or $CD8^+PD\text{-}1^+$ cytotoxic T cells. Additionally, two patients displayed close proximity to $CD3^+$ T cells expressing FOXP3 and pSMAD3, suggesting that regulatory T cells actively release TGF-β near tumor cells. This cluster was associated with favorable outcomes, including PFS over 6 months, OS over 12 months, high ISb and ISb_20 scores, and preserved HLA expression on $cytokeratin^+$ cells, except for 2 patients. Notably, these two patients were the only ones in this cluster with an OS of less than 12 months.

Median PFS was 6.58 months (95% CI: 4.18–not reached) for cluster 1 and 2.75 months (95% CI: 2.53–3.81) for cluster 2 (HR = 0.39, 95% CI: 0.15–1.00, p = 0.044) (Figure 5B). Median OS was 15.12 months (95% CI: 8.75–not reached) for cluster 1 and 6.07 months (95% CI: 4.41–12.7) for cluster 2 (HR = 0.31, 95% CI: 0.11–0.83, p = 0.015) (Figure 5C).

Univariate analysis indicated that higher densities of $CD3^+$ and $CD3^+CD8^-$ T cells, closer proximity of $CD3^+$ and $CD8^+$ T cells to tumor cells, and increased $CD45RO^+$ $CD8^+$ density and proximity were associated with better PFS (Figure 5D). Additionally, $PD\text{-}1^+$ cell density and the proximity of $CD3^+PD\text{-}1^+$ and $CD8^+PD\text{-}1^+$ cells to tumor cells were linked with improved OS (Figure 5E).

Analysis of paired samples collected at baseline, week 3, and week 11 showed no consistent increase or decrease in immune cell infiltration associated with response to treatment, *RAS*

Figure 3. Biopsy-adapted Immunoscore and efficacy results

(A–C) Representative immunofluorescence images of liver metastasis biopsies illustrating the 3 classes of biopsy-adapted Immunoscore (ISb) with blue for Hoechst (nuclei), pink for $CD3^+$, and orange for $CD8^+$: (A) ISb high, (B) ISb medium, and (C) ISb low. Scale bars: 100 μm.

(D and E) Kaplan-Meier survival curves for progression-free survival (PFS) and overall survival (OS) stratified by ISb levels (high, medium, and low). Tick marks represent censored patients. Log rank test p values are displayed.

(F–I) Bar plots showing the frequency distribution of patients based on ISb levels (high, medium, and low) and their (F) PFS status (≤6 vs. >6 months), (G) OS status (≤12 vs. >12 months), (H) cohort (*RAS*-MUT vs. *RAS*-WT), and (I) best overall response (BOR) status (tumor growth: increase of the size of the sum of target lesions; tumor shrinkage: decrease of the size of the sum of target lesions) across time points. Fisher's exact test p values are displayed.

(J–L) Forest plots from Cox proportional hazards (CoxPH) and linear regression multivariate models for (J) OS, (K) PFS, and (L) BOR, displaying hazard ratios (HRs and 95% CI) and regression coefficients (coef. and 95% CI) with p values for clinical covariates, including ISb.

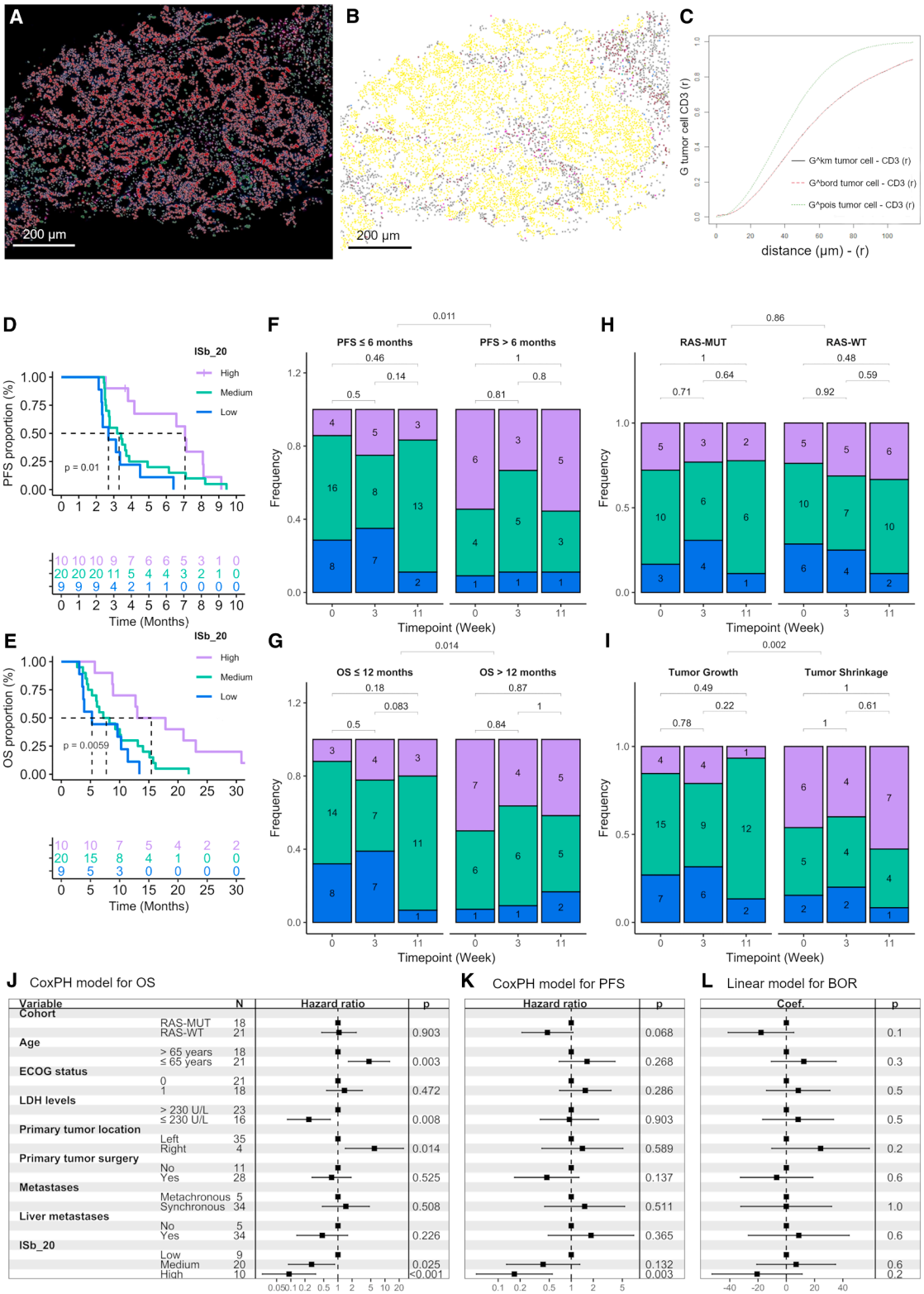

Figure 4. Distance-based biopsy-adapted Immunoscore (ISb_20) and clinical outcomes

(A) Representative immunofluorescence images of liver metastasis biopsies analyzed by HALO artificial intelligence module for the detection of tumor nuclei (red) and non-tumoral nuclei (green). Scale bars: 200 µm.

(legend continued on next page)

mutation status, BOR, patient survival, ISb, ISb_20, or HLA expression (Figure S3A). However, a slight decrease in PD-1 density was observed over time.

Using bulk RNA sequencing (RNA-seq), we further investigated the immune profiles of the two clusters (Figure 5F). Deconvolution analysis (consensus TME) demonstrated that cluster 1 had significantly higher infiltration of immune cell types derived from the consensus colon adenocarcinoma (COAD) gene lists compared to cluster 2 ($p < 0.001$) (Figure 5F). Notably, B cells ($p = 0.062$), cytotoxic cells ($p = 0.087$), mast cells ($p = 0.044$), NK cells ($p = 0.044$), $CD8^+$ T cells ($p = 0.087$), and overall immune score ($p = 0.074$) were higher in cluster 1 (Figure 5G). Differential expression analysis and gene set enrichment analysis (GSEA) on Gene Ontology (GO) and hallmark gene sets (Figures S3B–S3C) indicated that cluster 1 was enriched in hallmark inflammatory response and interferon-γ response pathways, as well as GO terms related to cytokine production, lymphocyte proliferation and activation, lymphocyte-mediated immunity, and immune response signaling, highlighting an immune-reactive profile in the baseline metastatic biopsies of these patients.

mRNA levels from baseline samples were further analyzed according to PFS duration (>6 vs. ≤ 6 months) (Figure S4). A total of 192 differentially expressed genes were identified, with those displaying an adjusted $p < 0.01$ shown on the heatmap. Unsupervised clustering revealed three distinct gene clusters and two patient clusters (A and B) (Figure S4A). Cluster A was associated with favorable clinical features, including BOR, iRECIST (PR or SD), PFS > 6 months, OS > 12 months, higher ISb, and higher ISb_20 scores. This cluster correlated with improved PFS ($p < 0.001$) (Figure S4B) and OS ($p = 0.003$) (Figure S4C). GSEA (Figure S4D) showed that hallmark gene lists related to allograft rejection, inflammatory response, and interferon-γ response were enriched in patients with PFS > 6 months. Conversely, pathways related to xenobiotic metabolism, fatty acid metabolism, bile acid metabolism, glycolysis, and oxidative phosphorylation were more prominent in patients with PFS ≤ 6 months, suggesting a tumor microenvironment less conducive to sustained immune activity. GO GSEA (Figure S4E) identified upregulated GO terms in patients with PFS > 6 months, including T and B lymphocyte activation, interleukin-12 production, lymphocyte proliferation and activation, antigen presentation, and chemotaxis, indicating a robust adaptive immune response. Pathway enrichment analysis using the Kyoto Encyclopedia of Genes and Genomes (KEGG) demonstrated the involvement of differentially expressed genes in immune pathways, including T cell receptor signaling, chemokine signaling, antigen processing and presentation, hematopoietic cell lineage, and the intestinal immune network for immunoglobulin (Ig)A production (data not shown). Overall, patients with PFS > 6 months exhibited a more active immune microenvironment, characterized by higher infiltration of T cells, closer proximity of immune cells to tumor cells, and elevated immune scores (ISb and ISb_20). Cluster 1, associated with prolonged PFS and OS, was enriched in adaptive immune pathways, including interferon-γ response, cytokine production, and antigen presentation, as revealed by RNA-seq and pathway analyses. In contrast, patients with PFS ≤ 6 months showed metabolic pathway enrichment, suggesting an immunosuppressive tumor microenvironment.

Immunoediting score is associated with patient survival, Immunoscore, and immune infiltration

Using whole-exome sequencing (WES) from 108 biopsies (41 patients), we derived the genetic immunoediting (GIE) score, which is the ratio of observed vs. expected numbers of neoantigens. We combined the GIE score with the immunologic constant of rejection (ICR) score[28] performed on bulk RNA-seq to perform a composite immunoediting score (IES) as previously described[29,30] (IES1 = ICR low and no GIE; IES2 = ICR low and GIE; IES3 = ICR high and no GIE; and IES4 = ICR high and GIE) (Figure 6).

At baseline, the distribution of IES categories was 11 biopsies (35.5%) in IES4, 6 (19.4%) in IES3, 4 (12.9%) in IES2, and 10 (32.3%) in IES1. Median PFS for IES4 to IES1 categories was 4.93 (95% CI: 3.19–not reached), 3.62 (95% CI: 2.53–not reached), 2.60 (95% CI: 2.14–not reached), and 2.66 (95% CI: 2.33–not reached) months, respectively ($p = 0.02$) (Figure 6A). Median OS for IES categories 4, 3, 2, and 1 was 10.03 (95% CI: 8.25–30.9), 7.07 (95% CI: 4.18–not reached), 4.16 (95% CI: 3.78–not reached), and 6.85 (95% CI: 4.14–not reached) months, respectively ($p = 0.04$) (Figure 6B).

Like ISb and ISb_20, there were no significant changes in IES proportions over time (weeks 0, 3, and 11) (Figures 6C–6F). A higher proportion of IES4 was associated with longer PFS (>6 months), longer OS (>12 months), and tumor shrinkage, though it was not associated with *RAS* mutation status. In multivariate models adjusted for OS, PFS, and BOR, IES4 was trendily associated with better OS (HR = 0.37, 95% CI: 0.12–1.16, $p = 0.09$) and significantly associated with improved PFS

(B) Representative dot plot reconstitution of a liver metastasis biopsy with tumor cells in yellow, $CD3^+CD8^-$ T cells in maroon, $CD3^+CD8^+$ T cells in pink, and stromal unstained cells in gray.

(C) Illustrated representative G-cross analysis of the probability distribution of $CD3^+$ T cells near tumor cells, with the *y* axis representing the probability of a $CD3^+$ T cells being at a given radius (r) (*x* axis) of a tumor cell. G^{km} (solid black line) represents the interaction function for tumor cells measured against $CD3^+$ T cells, G^{bord} (dashed red line) indicates the border-corrected function, and G^{pois} (green line) illustrates the function under the assumption of a homogeneous Poisson process (independent, random distribution), serving as baseline comparison. The probability value of the G^{km} function at 20 μm of distance for $CD3^+$ T and $CD8^+$ T cells has been used to compute a distance-based biopsy-adapted Immunoscore (ISb_20).

(D and E) Kaplan-Meier survival curves for progression-free survival (PFS) and overall survival (OS) stratified by ISb_20 levels (high, medium, and low). Tick marks represent censored patients. Log rank test *p* values are displayed.

(F–I) Bar plots showing the frequency distribution of patients based on ISb_20 levels (high, medium, and low) and their (F) PFS status (≤6 vs. >6 months), (G) OS status (≤12 vs. >12 months), (H) cohort (*RAS*-MUT vs. *RAS*-WT), and (I) best overall response (BOR) status (tumor growth: increase of the size of the sum of target lesions; tumor shrinkage: decrease of the size of the sum of target lesions) across time points. Fisher's exact test *p* values are displayed.

(J–L) Forest plots from Cox proportional hazards (CoxPH) and linear regression multivariate models for (J) OS, (K) PFS, and (L) BOR, displaying hazard ratios (HRs and 95% CI) and regression coefficients (coef. and 95% CI) with *p* values for clinical covariates, including ISb_20.

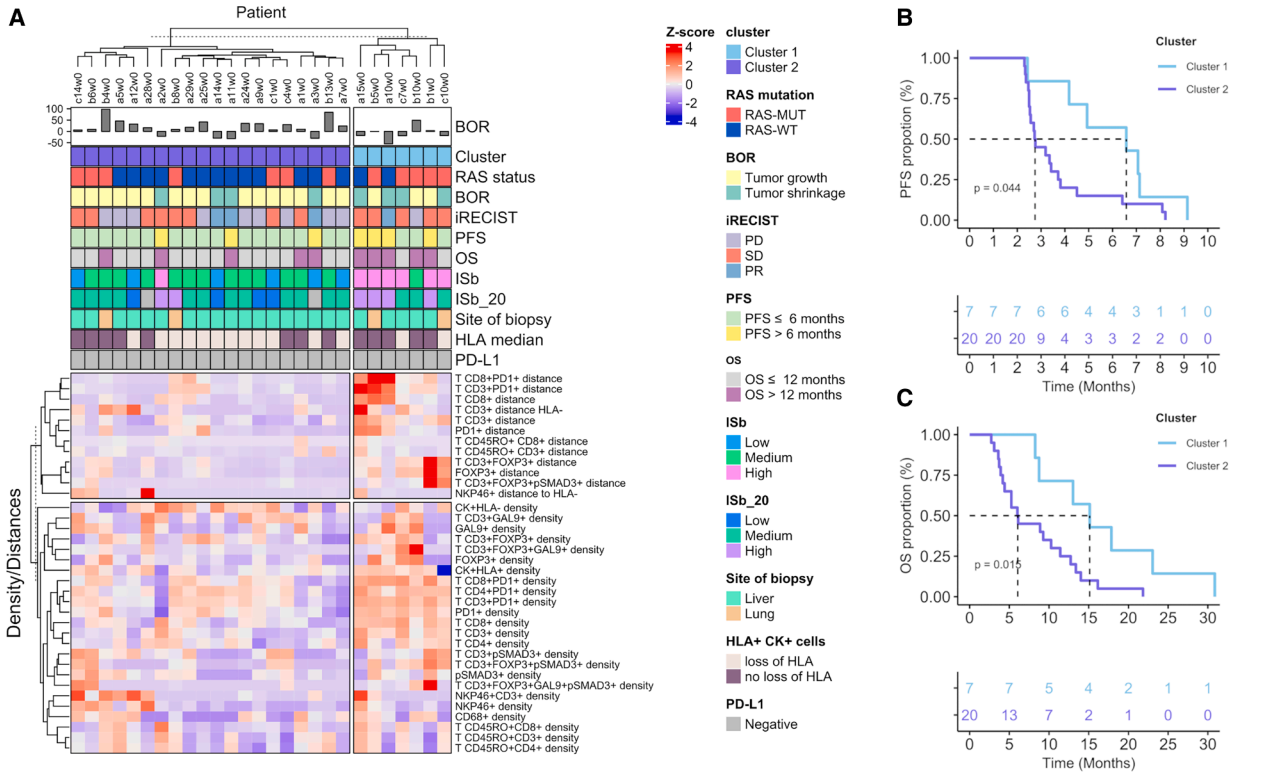

D Univariate CoxPH for PFS

Variable	HR (95% CI)	p-value
T CD3+ density	0.37 (0.20-0.67)	0.001
T CD4+ density	0.47 (0.28-0.79)	0.005
T CD3+ distance	0.50 (0.30-0.81)	0.005
T CD8+ distance	0.60 (0.38-0.95)	0.029
PD1+ density	0.88 (0.63-1.25)	0.480
T CD3+PD1+ distance	0.71 (0.50-1.01)	0.058
T CD8+PD1+ distance	0.75 (0.54-1.06)	0.109
T CD45RO+ CD8+ density	0.64 (0.41-1.00)	0.050
T CD45RO+ CD8+ distance	0.10 (0.01-1.00)	0.050

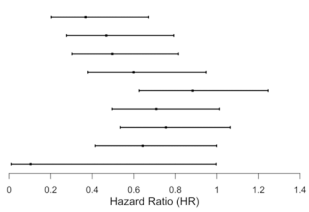

E Univariate CoxPH for OS

HR (95% CI)	p-value
0.62 (0.36-1.05)	0.077
0.71 (0.41-1.22)	0.209
0.56 (0.33-0.95)	0.031
0.59 (0.36-0.96)	0.034
0.68 (0.46-1.00)	0.047
0.67 (0.45-1.00)	0.049
0.65 (0.42-0.98)	0.041
0.75 (0.48-1.18)	0.214
0.24 (0.04-1.61)	0.143

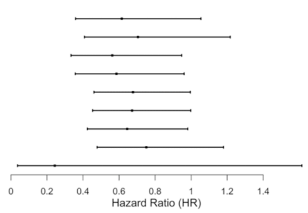

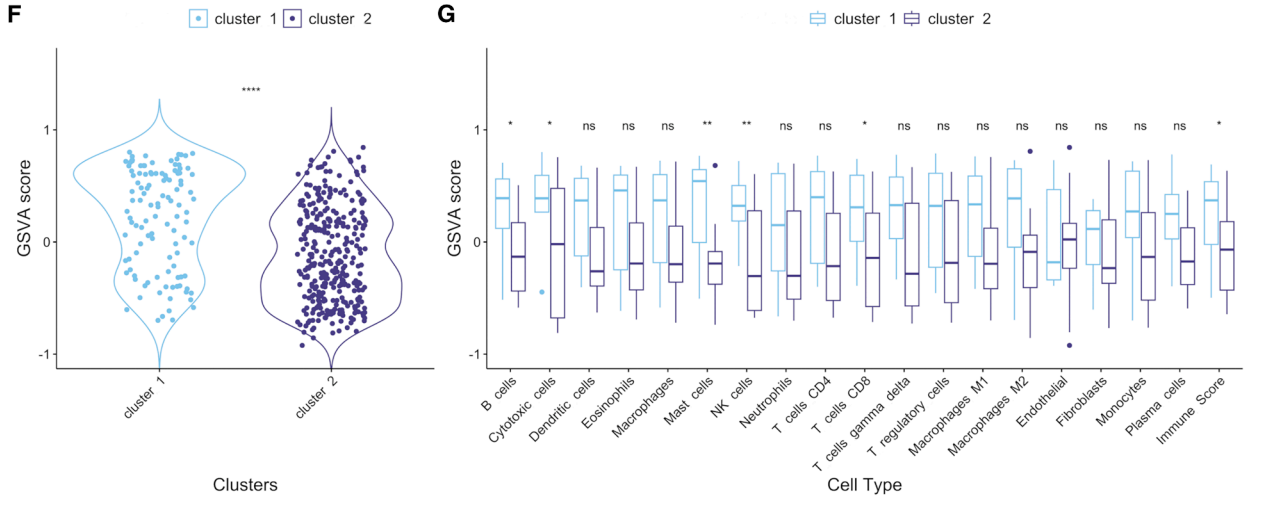

(legend on next page)

(HR = 0.31, 95% CI: 0.10–0.96, $p = 0.04$) (Figures 6H and 6I). IES scores at each time point, along with *RAS* mutation status, BOR, PFS, OS, ISb, and ISb_20 classifications, are shown in Figure S5.

When comparing IES with ISb and ISb_20, most ISb-high or ISb_20-high samples were associated with an adaptive immune signature and GIE and classified as IES4 (Figures S6A and S6B). ISb-medium or ISb_20-medium samples included a range of IES1 to IES4, while ISb-low or ISb_20-low samples were mostly without GIE and classified as IES1–IES3. At baseline, week 3, and week 11, 3 (20.0%), 2 (15.4%), and 2 (18.2%) biopsies, respectively, were classified as high across all three scores (ISb high, ISb_20 high, and IES4) (Figures S6C–S6E). In contrast, 6 (40.0%), 6 (46.2%), and 5 (45.5%) biopsies at these time points were classified as IES4 alone. Notably, ISb showed the highest overlap with the other scores, suggesting it may be the most integrative or comprehensive measure of immune activity among the three scores.

Finally, when comparing mIF-defined clusters, we observed that cluster 1 was consistently enriched for high ISb and ISb_20 scores across all time points, indicating a persistently active immune profile. In contrast, cluster 2 predominantly exhibited lower IES scores (IES1–IES3), reflective of a less immunogenic environment (Figures S7A–S7C). Figures S7D–S7F further illustrate the overlap between ISb high, ISb_20 high, IES4, and cluster classifications at baseline, week 3, and week 11.

Genomic landscape and altered signaling pathways

The genomic landscape of 108 biopsies from 41 patients is characterized in Figure 7. Missense mutations and single-nucleotide polymorphisms (SNPs) were the most frequent variant types observed. *APC* (73%), *TP53* (60%), *TTN* (53%), *KRAS* (39%), and *MUC16* (24%) were the top five mutated genes (Figure 7A). The most frequently altered pathways included WNT (89%), RTK-RAS (receptor tyrosine kinase-RAS) (70%), Hippo (56%), NOTCH (46%), PI3K (19%), TGF-β (15%), and cell cycle (6%) (Figure 7A, pathways). Within the RTK-RAS pathway, the most commonly mutated genes were *KRAS* (39%), *PIK3CA* (PI3K/mTOR pathway) (8%), *JAK2* (JAK-STAT pathway) (7%), *RASAL2* (6%), and *ERBB4* (6%).

In the *RAS* WT cohort (cohort A), 56.36% of samples showed alterations in the RTK-RAS pathway, with notable mutations in *ERBB4* (11%), *BRAF* (9%), *KRAS* (7%), *PDGFRB* (7%), and *ALK* (5%) (Figure 7A, right). Interestingly, some of these were already observed at baseline, and a few of these mutations emerged after treatment initiation, suggesting a possible adaptive resistance mechanism to anti-EGFR treatment received prior to or during study treatment. The median TMB observed in the metastasis biopsies (median mutation per Mb = 3.03) was close to the COAD cohort of The Cancer Genome Atlas (TCGA) (Figure 7B). Conversely to the COAD cohort, the metastatic samples did not exhibit a "tail" of highly mutated tumors, probably due to the exclusion of MSI-H tumors from our study.

Finally, no significant associations were identified between the mutational profiles of these biopsies and patient outcomes, such as PFS, OS, or BOR, indicating that mutational burden and gene alterations alone may not predict response or survival in this study.

DISCUSSION

Treatment of patients with refractory MSS mCRC remains a significant clinical challenge. The efficacy of available therapies is limited, and patient outcomes are generally poor.[31–34] To date, ICIs have shown limited effectiveness in this patient population.[35,36] Mechanisms of resistance may involve several factors, including the downregulation of major histocompatibility complex (MHC) class I, a low TMB, or tumor-induced microenvironmental changes, resulting in immune desertification or the presence of an immune-excluded or immune-suppressed tumor phenotype.[37]

Cetuximab has been shown to induce an immune response involving both innate and adaptive components that may synergize with ICIs.[23,25,38] In the AVETUXIRI trial, which recruited 55 patients with MSS mCRC refractory to chemotherapy, we observed a manageable safety profile. Although the prespecified efficacy endpoints were not reached, the median PFS of the *RAS* WT cohort (3.7 months) was comparable to that of the ctDNA *RAS*/*BRAF* WT cohort of the CAVE trial (4.0 months), which evaluated avelumab and cetuximab as a third-line rechallenge therapy.[39] However, the median OS (10.8 months) was lower than in the CAVE trial (17.8 months). Notably, the CAVE trial demonstrated superior efficacy compared to regorafenib[32] (receptor tyrosine kinase inhibitor), trifluridine/tipiracil[31] (thymidine phosphorylase inhibitor), and fruquintinib[33] (kinase inhibitor), supporting the ongoing investigation of this combination in the CAVE-2 trial.[40] The response rate (21.4%) was higher than that of the CAVE trial (7.8%) and similar to the results in patients treated with cetuximab and irinotecan in the CRICKET trial (21%).[41]

Figure 5. Comprehensive analysis of the tumor immune microenvironment

(A) Heatmap of clinical and immune characteristics across baseline metastasis biopsies. The heatmap annotations show clinical variables including best overall response (BOR), displayed as both a continuous and discrete variable (tumor growth: increase in the size of target lesions; tumor shrinkage: decrease in target lesions), *RAS* mutation status, iRECIST criteria, progression-free survival (PFS), overall survival (OS), ISb, ISb_20, site of biopsy, HLA^+CK^+ double-positive staining (HLA loss defined as staining below the median; no HLA loss above the median), and PD-L1 status (negative when there are <1% $PD\text{-}L1^+$ cells, positive when there are ≥1% $PD\text{-}L1^+$ cells). The bottom image presents immune-related density and distance probability at 20-μm features as *Z* scores for multiple cell populations. Biopsies were stratified into two clusters using unsupervised Euclidean distance clustering.

(B and C) Kaplan-Meier survival curves for (B) PFS and (C) OS, stratified by clusters with tick marks indicating censored patients. The number of patients at risk is displayed below each plot. Log rank test *p* values are indicated.

(D and E) Forest plots from univariate Cox proportional hazards (CoxPH) analysis of immune cell populations. (D) shows immune features associated with PFS and (E) with OS. Hazard ratios (HRs) and 95% CI are displayed.

(F and G) Bulk RNA-seq gene set variation analysis (GSVA) scores of immune cell types from the consensus tumor microenvironment (consensus TME) colon adenocarcinoma (COAD) dataset. (F) Violin plot comparing GSVA scores for all cell types combined between mIF clusters and (G) boxplot displaying GSVA scores for individual cell types. $^*p < 0.1$, $^{**}p < 0.05$, and $^{***}p < 0.001$. Non-significant differences are marked "ns." Statistical analysis was performed using t tests and Wilcoxon tests.

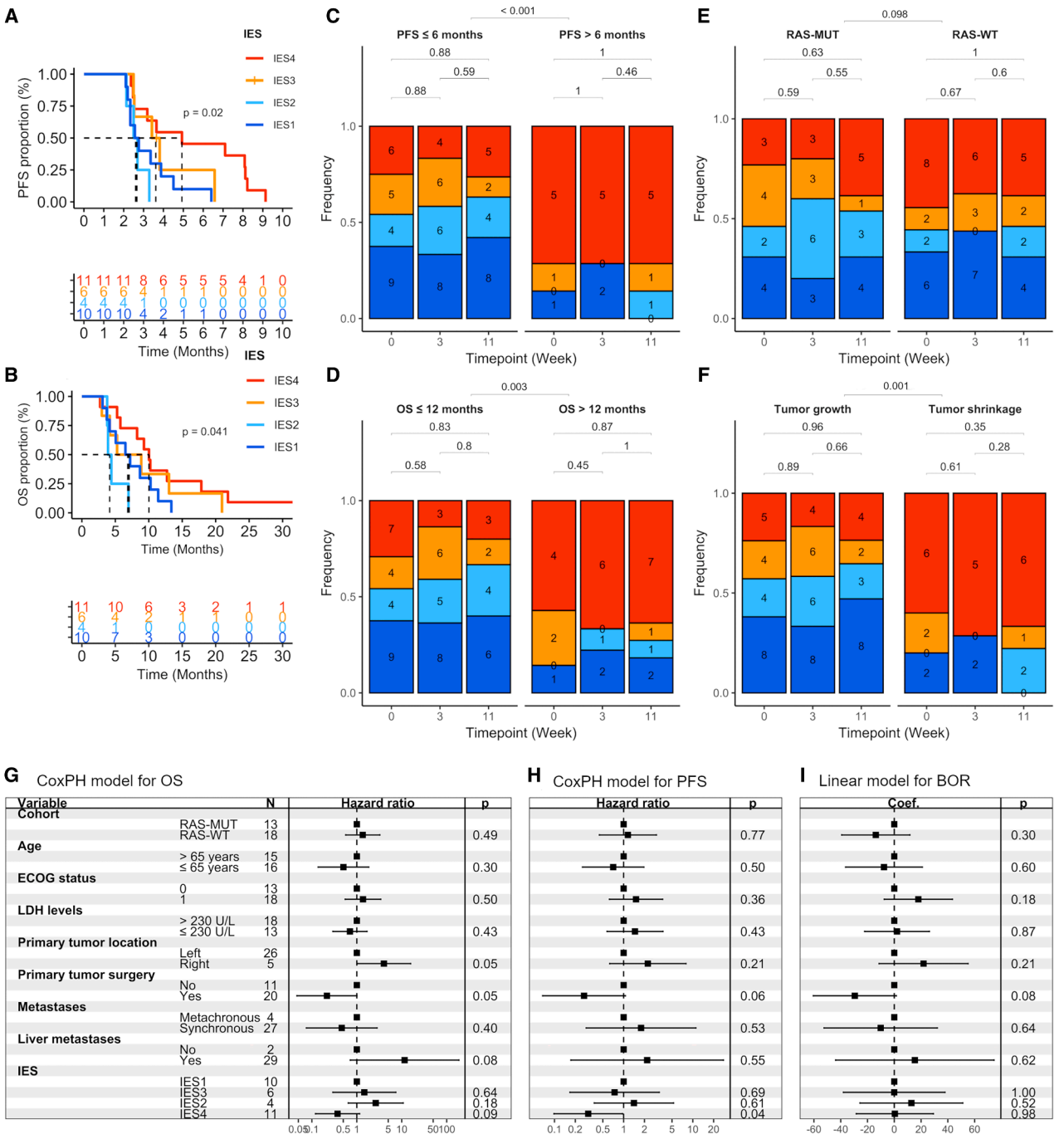

Figure 6. Immunoediting score and clinical outcomes

(A and B) Kaplan-Meier survival curves for progression-free survival (PFS) and overall survival (OS) stratified by immunoediting score (IES), based on both genetic immunoediting (GIE) and immunologic constant of rejection (ICR) (IES1 = ICR low and no GIE; IES2 = ICR low and GIE; IES3 = ICR high and no GIE; and IES4 = ICR high and GIE). Tick marks represent censored patients. The number of patients at risk is displayed below each plot. Log rank test *p* values are displayed.

(C–F) Bar plots showing the frequency distribution of patients based on IES and their (C) PFS status (≤6 vs. >6 months), (D) OS status (≤12 vs. >12 months), (E) cohort, and (F) best overall response (BOR) status (tumor growth: increase of the size of the sum of target lesions; tumor shrinkage: decrease of the size of the sum of target lesions) across time points. Fisher's exact test *p* values are displayed.

(G–I) Forest plots from Cox proportional hazards (CoxPH) and linear regression multivariate models for (G) OS, (H) PFS, and (I) BOR (as a continuous variable), displaying hazard ratios (HRs and 95% CI) and regression coefficients (coef. and 95% CI) with *p* values for clinical covariates, including IES.

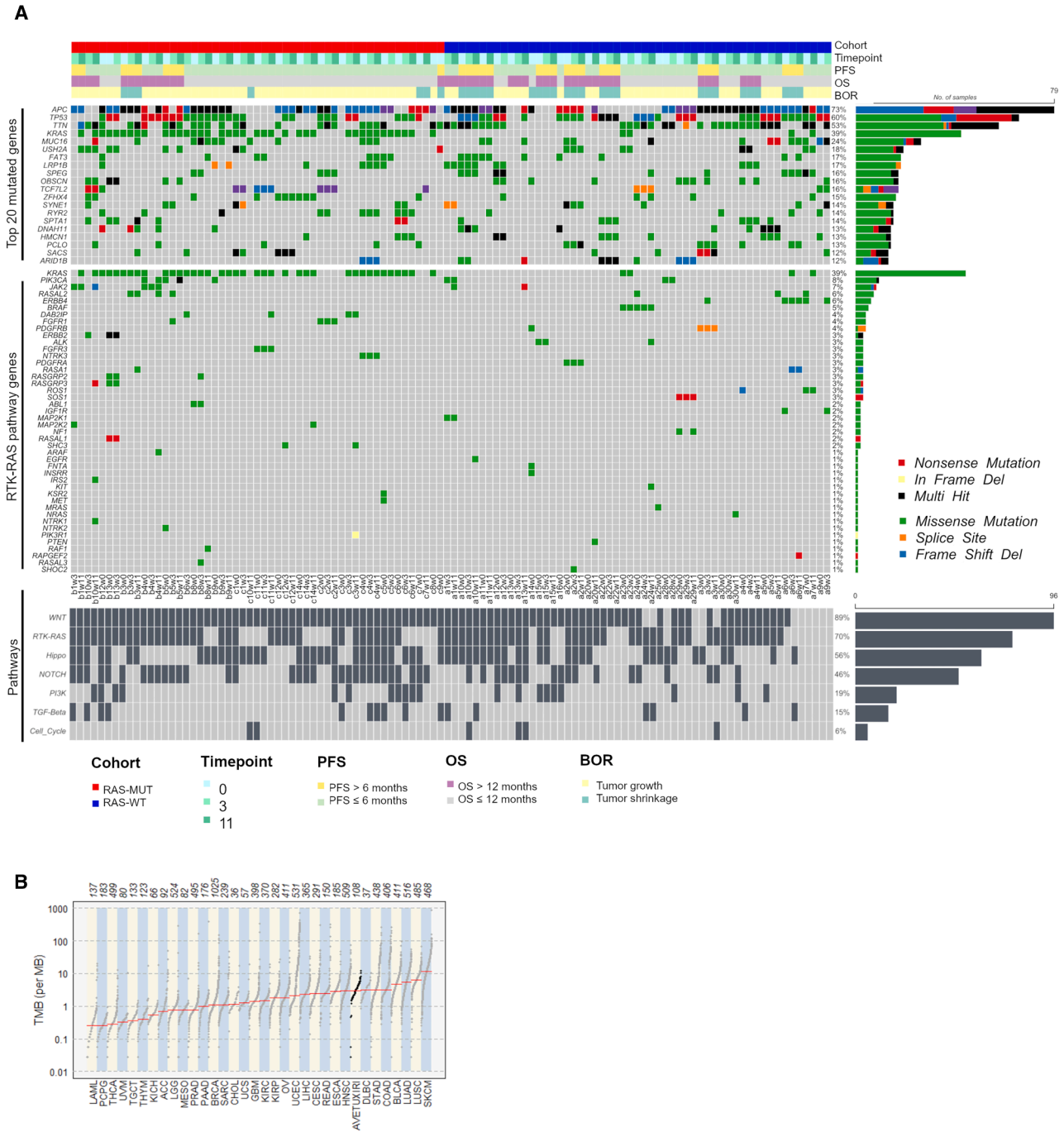

Figure 7. Mutational landscape and tumor mutational burden across time points in *RAS*-MUT and *RAS*-WT cohorts

(A) Oncoplot displaying the top 20 mutated genes and RTK-*RAS* pathway genes across baseline (week 0), week 3, and week 11 in *RAS*-MUT and *RAS*-WT cohorts. Each column represents a patient, with mutations color coded according to mutation type: nonsense mutation (red), in-frame deletion (black), multi-hit mutation (yellow), missense mutation (green), splice site mutation (blue), and frameshift deletion (orange). The upper annotation bars display patient cohort (*RAS*-MUT and *RAS*-WT), time point, progression-free survival (PFS; ≤6 vs. >6 months), overall survival (OS; ≤12 vs. >12 months), and best overall response (BOR; tumor growth or shrinkage). The pathway row represents the most altered pathway with gray when at least one gene is mutated in the pathway. The bar plot on the right shows the mutation frequency of each gene.

(B) Line plot of tumor mutational burden (TMB) per Mb across patients, ranked by TMB levels. TMB values are shown on a log scale. Patients are grouped by cohort (*RAS*-MUT and *RAS*-WT) and time point (weeks 0, 3, and 11), with color shading indicating the time point.

Unlike these studies, AVETUXIRI was not an anti-EGFR rechallenge trial. All patients enrolled were heavily pre-treated (a median of 3.5 prior lines of therapy) and had primary or acquired resistance to anti-EGFR therapy. Notably, 60.7% of patients were progressing on this treatment just before trial inclusion. In addition, post hoc WES analysis of baseline metastatic biopsies revealed that, among the 28 patients initially classified as *RAS* WT, *RAS* or *BRAF* mutations were detected in 4 patients and RTK-RAS pathway alterations in up to 50% of the cohort. No response (RECIST1.1) was observed in the *RAS* MUT cohort. PFS and OS of this cohort were comparable to those of regorafenib, trifluridine/tipiracil, or fruquintinib (treatment used in similar indication)[31–33] but lower than those of trifluridine/tipiracil combined with bevacizumab (anti-VEGF-A).[34] Considering the higher response rate (up to 30%) and survival observed with anti-EGFR treatment in rechallenge trials excluding *RAS* and *BRAF* mutations detected in liquid biopsies,[31–34,41–44] it is possible that the efficacy results of the *RAS* WT cohort would have been different if we had planned to do the same at study entry since, from a statistical point of view, only one patient with a PR missed (6 observed instead of 7 required) reaching primary efficacy endpoint.

The AVETUXIRI trial was initially designed as a proof-of-concept study to induce and select immunogenic tumors likely to benefit from ICI-based treatment while longitudinally monitoring changes in the immune microenvironment through metastatic biopsies. Unexpectedly, the 2-week induction treatment with cetuximab and irinotecan before initiating avelumab did not induce a significant tumor immune response over time, as evidenced by the lack of substantial changes in the immune microenvironment from baseline to weeks 3 and 11. In contrast, we observed that patients with tumor immune reactivity in baseline metastatic biopsies benefited from the study treatment with an increase in survival. Using mIF analysis, we reported that an ISb quantifying CD3 and CD8 T cell densities[26] correlated with increased PFS (ISb high vs. low: HR = 0.24, $p = 0.007$) and OS (ISb high vs. low: HR = 0.44, $p = 0.09$) in the whole study population, independently of the presence of *RAS* mutation. These observations are in line with the preliminary results from the POCHI trial, which is prospectively evaluating first-line treatment with pembrolizumab (anti-PD-1) and chemotherapy for patients with mCRC with a high Immunoscore in resected primary CRC.[45] An impressive 17% complete response rate and encouraging survival results justify the current pursuit of this study. Due to the lack of PD-L1 staining in mCRC metastases, we were unable to implement the Immunoscore-IC showing predictive efficacy for ICI treatment in primary tumors.[16,17] Recent studies reported that a tumor PD-L1 expression ($\geq$1% of cells) was observed only in 4%–10% (depending on the staining antibody) of the resected CRC tumors[46] and was highly heterogeneous in time and space[47] and lower in MSS mCRC compared to MSI-H and other cancers.[48] Therefore, we implemented a distance-based ISb (ISb_20) as an alternative to capture the spatial relationship between immune cells and tumor cells. Similarly to ISb, patients with a baseline ISb_20 high exhibited better PFS (HR = 0.24, $p = 0.004$) and OS (HR = 0.20, $p = 0.003$) in all cohorts of patients.

In addition, unsupervised clustering analysis integrating all immune cell densities and distance revealed an immunogenic cluster enriched in ISb and ISb_20 and increased density and proximity of activated T cells ($CD3^+PD1^+$, $CD4^+PD1^+$, and $CD8^+PD1^+$). This cluster was associated with favorable survival, as reported in other trials for PD-(L)1 blockade in MSI-H[49] and MSS mCRC.[16,45,50] Higher density and tumor proximity were also noted for $FOXP3^+$ cells. Although their role remains complex and controversial, studies have indicated that they could be linked to favorable outcomes in CRC.[38,51,52] Further supported by RNA-seq analysis, these results suggested, collectively, that the identification of an activated adaptive anti-tumor immune microenvironment could be a biomarker of interest. We observed that ~35% of baseline biopsies from included patients had a high composite IES (IES4)[29] and could identify patients able to benefit from ICIs (increased PFS and OS). The ISb-high and ISb_20-high samples overlapped with IES4 classification, while ~40% of the IES4 samples were not classified as ISb high or ISb_20 high. The ISb showing the highest overlap could be the most integrative measure of the anti-tumor immune activity. Thus, an appropriate pre-existing immune contexture at the start of the treatment (baseline) can provide the license for immunotherapy to be effective.

In conclusion, although the efficacy endpoints were not met globally, our study generated comprehensive, high-resolution data on the tumor microenvironment, revealing potential biomarkers of benefit from immunotherapy. Notably, our findings highlight that an anti-tumor immune reactiveness, reflected by high Immunoscores within the baseline CRC metastases biopsies, could be a predictive biomarker of efficacy for avelumab-based treatment in the metastatic setting.

Limitations of the study

The limitations of our study arise from its design as a small, single-arm, phase 2, proof-of-concept trial that lacks a control arm without avelumab or cetuximab. This approach presented challenges, including testing the hypothesis that cetuximab could stimulate an immune response, particularly in MSS *RAS*-mutated mCRC, a subset typically resistant to treatments. Moreover, our results should be validated in controlled, prospective trials that select immunogenic mCRC (as determined by high Immunoscores) that are likely to benefit from ICI-based treatments, as planned in the POCHI trial[45] and the upcoming AtezoTRIBE-2 study.[16] Ultimately, further large-scale randomized studies are necessary to determine the predictive or prognostic value of our findings.[53–56]

RESOURCE AVAILABILITY

Lead contact

Further information and requests for resources and reagents should be directed to and will be fulfilled by the lead contact, Pr. Marc Van den Eynde (marc.vandeneynde@uclouvain.be).

Materials availability

This study did not generate new unique reagents.

Data and code availability

- Anonymized bulk RNA-seq raw-count matrix, WES variant calling format (VCF) files, mutation annotation format (MAF) files, and a clinical data table were deposited at Mendeley Data and are publicly available

as of the date of publication (Mendeley Data: https://doi.org/10.17632/ffb35993tw.1). The accession numbers are listed in the key resources table.

- All original codes have been deposited at Mendeley Data (https://doi.org/10.17632/ffb35993tw.1) and are publicly available on the date of publication.
- Any additional information required to reanalyze the data reported in this paper is available from the lead contact upon request.

ACKNOWLEDGMENTS

This study received a fixed grant and drug supply of avelumab and cetuximab by the healthcare business of Merck KGaA, Darmstadt, Germany (CrossRef Funder ID: 10.13039/100009945). This study received Sidra Medicine funding (SDR400029). N.H. was supported by a grant from the Belgian National Fund for Scientific Research (Télévie/FNRS 7460918F). E.B. was supported by a grant from the Belgian National Fund for Scientific Research (Télévie/FNRS 7.4600.23). The authors would like to acknowledge the Sidra Medicine research branch core facilities, and our research administration teams without whom we could not have performed this work.

AUTHOR CONTRIBUTIONS

N.H. and E.B. are both main authors and contributed equally to the work. M.V.d.E. conceived the trial and was the coordinating investigator and principal investigator at the Cliniques Universitaires St-Luc. W.H. was the principal investigator on the Sidra Medicine side. M.V.d.E. and W.H. are both corresponding authors. J.G. contributed to the conception of the trial together with M.V.d.E. C.B. and F.M.O. contributed to mIF stainings. F.V., T.M., W.H., and D.B. contributed to the RNA-seq, WES, variant calling, and ICR scoring. L.F. and M.C. performed the GIE score analysis. R.H., N.v.B., and S.B. contributed to bioinformatics analysis. A.v.M. contributed to statistical analysis. I.S., A.D.C., and J.C. contributed to the inclusion of patients, their study treatment, and clinical follow-up. Metastases biopsies were collected by P.G. and B.G. M.-L.C. was the clinical research associate of the trial.

DECLARATION OF INTERESTS

The authors declare no conflicts of interest.

STAR★METHODS

Detailed methods are provided in the online version of this paper and include the following:

- KEY RESOURCES TABLE
- EXPERIMENTAL MODEL AND SUBJECT DETAILS
  - Study design and participants
- METHOD DETAILS
  - Procedures
  - Outcomes and statistical considerations
  - Sample processing
  - Multiplex immunofluorescence
  - Gene expression
  - Whole exome sequencing
  - IES classification and analysis
- QUANTIFICATION AND STATISTICAL ANALYSIS
  - Genetic immunoediting value
  - G-cross function
  - Statistics
- ADDITIONAL RESOURCES

SUPPLEMENTAL INFORMATION

Supplemental information can be found online at https://doi.org/10.1016/j.xcrm.2025.102201.

Received: December 19, 2024
Revised: March 21, 2025
Accepted: May 29, 2025
Published: June 24, 2025

REFERENCES

1. Bray, F., Laversanne, M., Sung, H., Ferlay, J., Siegel, R.L., Soerjomataram, I., and Jemal, A. (2024). Global cancer statistics 2022: GLOBOCAN estimates of incidence and mortality worldwide for 36 cancers in 185 countries. CA Cancer J. Clin. *74*, 229–263. https://doi.org/10.3322/caac.21834.
2. Cervantes, A., Adam, R., Roselló, S., Arnold, D., Normanno, N., Taïeb, J., Seligmann, J., De Baere, T., Osterlund, P., Yoshino, T., et al. (2023). Metastatic colorectal cancer: ESMO Clinical Practice Guideline for diagnosis, treatment and follow-up. Ann. Oncol. *34*, 10–32. https://doi.org/10.1016/j.annonc.2022.10.003.
3. Benson, A.B., Venook, A.P., Adam, M., Chang, G., Chen, Y.J., Ciombor, K.K., Cohen, S.A., Cooper, H.S., Deming, D., Garrido-Laguna, I., et al. (2024). Colon Cancer, Version 3.2024, NCCN Clinical Practice Guidelines in Oncology. J. Natl. Compr. Canc. Netw. *22*, e240029. https://doi.org/10.6004/jnccn.2024.0029.
4. Douillard, J.Y., Oliner, K.S., Siena, S., Tabernero, J., Burkes, R., Barugel, M., Humblet, Y., Bodoky, G., Cunningham, D., Jassem, J., et al. (2013). Panitumumab-FOLFOX4 treatment and RAS mutations in colorectal cancer. N. Engl. J. Med. *369*, 1023–1034. https://doi.org/10.1056/NEJMoa1305275.
5. Arnold, D., Lueza, B., Douillard, J.Y., Peeters, M., Lenz, H.J., Venook, A., Heinemann, V., Van Cutsem, E., Pignon, J.P., Tabernero, J., et al. (2017). Prognostic and predictive value of primary tumour side in patients with RAS wild-type metastatic colorectal cancer treated with chemotherapy and EGFR directed antibodies in six randomized trials. Ann. Oncol. *28*, 1713–1729. https://doi.org/10.1093/annonc/mdx175.
6. Le, D.T., Durham, J.N., Smith, K.N., Wang, H., Bartlett, B.R., Aulakh, L.K., Lu, S., Kemberling, H., Wilt, C., Luber, B.S., et al. (2017). Mismatch repair deficiency predicts response of solid tumors to PD-1 blockade. Sci. Technol. Humanit. *357*, 409–413. https://doi.org/10.1126/science.aan6733.
7. Andre, T., Shiu, K.K., Kim, T.W., Jensen, B.V., Jensen, L.H., Punt, C., Smith, D., Garcia-Carbonero, R., Benavides, M., Gibbs, P., et al. (2020). Pembrolizumab in Microsatellite-Instability-High Advanced Colorectal Cancer. N. Engl. J. Med. *383*, 2207–2218. https://doi.org/10.1056/NEJMoa2017699.
8. Lenz, H.J., Van Cutsem, E., Luisa Limon, M., Wong, K.Y.M., Hendlisz, A., Aglietta, M., García-Alfonso, P., Neyns, B., Luppi, G., Cardin, D.B., et al. (2022). First-Line Nivolumab Plus Low-Dose Ipilimumab for Microsatellite Instability-High/Mismatch Repair-Deficient Metastatic Colorectal Cancer: The Phase II CheckMate 142 Study. J. Clin. Oncol. *40*, 161–170. https://doi.org/10.1200/JCO.21.01015.
9. Chalabi, M., Fanchi, L.F., Van den Berg, J.G., Beets, G.L., Lopez-Yurda, M., Aalbers, A.G., Grootscholten, C., Snaebjornsson, P., Maas, M., Mertz, M., et al. (2018). Neoadjuvant ipilimumab plus nivolumab in early stage colon cancer [ESMO abstract LBA37_PR]. Ann. Oncol. *29*, 731.
10. Giannakis, M., Mu, X.J., Shukla, S.A., Qian, Z.R., Cohen, O., Nishihara, R., Bahl, S., Cao, Y., Amin-Mansour, A., Yamauchi, M., et al. (2016). Genomic Correlates of Immune-Cell Infiltrates in Colorectal Carcinoma. Cell Rep. *15*, 857–865. https://doi.org/10.1016/j.celrep.2016.03.075.
11. Binnewies, M., Roberts, E.W., Kersten, K., Chan, V., Fearon, D.F., Merad, M., Coussens, L.M., Gabrilovich, D.I., Ostrand-Rosenberg, S., Hedrick, C.C., et al. (2018). Understanding the tumor immune microenvironment (TIME) for effective therapy. Nat. Med. *24*, 541–550. https://doi.org/10.1038/s41591-018-0014-x.
12. Huyghe, N., Benidovskaya, E., Stevens, P., and Van den Eynde, M. (2022). Biomarkers of Response and Resistance to Immunotherapy in Microsatellite Stable Colorectal Cancer: Toward a New Personalized Medicine. Cancers (Basel) *14*, 2241. https://doi.org/10.3390/cancers14092241.
13. Domingo, E., Freeman-Mills, L., Rayner, E., Glaire, M., Briggs, S., Vermeulen, L., Fessler, E., Medema, J.P., Boot, A., Morreau, H., et al. (2016).

Somatic POLE proofreading domain mutation, immune response, and prognosis in colorectal cancer: a retrospective, pooled biomarker study. Lancet Gastroenterol. Hepatol. *1*, 207–216. https://doi.org/10.1016/S2468-1253(16)30014-0.

14. Mo, S., Ma, X., Li, Y., Zhang, L., Hou, T., Han-Zhang, H., Qian, J., Cai, S., Huang, D., and Peng, J. (2020). Somatic POLE exonuclease domain mutations elicit enhanced intratumoral immune responses in stage II colorectal cancer. J. Immunother. Cancer *8*, e000881. https://doi.org/10.1136/jitc-2020-000881.
15. Wang, F., Zhao, Q., Wang, Y.N., Jin, Y., He, M.M., Liu, Z.X., and Xu, R.H. (2019). Evaluation of POLE and POLD1 Mutations as Biomarkers for Immunotherapy Outcomes Across Multiple Cancer Types. JAMA Oncol. *5*, 1504–1506. https://doi.org/10.1001/jamaoncol.2019.2963.
16. Antoniotti, C., Rossini, D., Pietrantonio, F., Salvatore, L., Lonardi, S., Tamberi, S., Marmorino, F., Moretto, R., Prisciandaro, M., Tamburini, E., et al. (2024). Upfront Fluorouracil, Leucovorin, Oxaliplatin, and Irinotecan Plus Bevacizumab With or Without Atezolizumab for Patients With Metastatic Colorectal Cancer: Updated and Overall Survival Results of the ATEZOTRIBE Study. J. Clin. Oncol. *42*, 2637–2644. https://doi.org/10.1200/JCO.23.02728.
17. Ghiringhelli, F., Bibeau, F., Greillier, L., Fumet, J.D., Ilie, A., Monville, F., Laugé, C., Catteau, A., Boquet, I., Majdi, A., et al. (2023). Immunoscore immune checkpoint using spatial quantitative analysis of CD8 and PD-L1 markers is predictive of the efficacy of anti- PD1/PD-L1 immunotherapy in non-small cell lung cancer. EBioMedicine *92*, 104633. https://doi.org/10.1016/j.ebiom.2023.104633.
18. Huyghe, N., Baldin, P., and Van den Eynde, M. (2020). Immunotherapy with immune checkpoint inhibitors in colorectal cancer: what is the future beyond deficient mismatch-repair tumours? Gastroenterol. Rep. *8*, 11–24. https://doi.org/10.1093/gastro/goz061.
19. Grasso, C.S., Giannakis, M., Wells, D.K., Hamada, T., Mu, X.J., Quist, M., Nowak, J.A., Nishihara, R., Qian, Z.R., Inamura, K., et al. (2018). Genetic Mechanisms of Immune Evasion in Colorectal Cancer. Cancer Discov. *8*, 730–749. https://doi.org/10.1158/2159-8290.CD-17-1327.
20. Baraibar, I., Mirallas, O., Saoudi, N., Ros, J., Salvà, F., Tabernero, J., and Élez, E. (2021). Combined Treatment with Immunotherapy-Based Strategies for MSS Metastatic Colorectal Cancer. Cancers (Basel) *13*, 6311. https://doi.org/10.3390/cancers13246311.
21. Germani, M.M., and Moretto, R. (2021). Immune Checkpoint Inhibitors in Mismatch Repair Proficient/Microsatellite Stable Metastatic Colorectal Cancer Patients: Insights from the AtezoTRIBE and MAYA Trials. Cancers (Basel) *14*, 52. https://doi.org/10.3390/cancers14010052.
22. Srivastava, R.M., Trivedi, S., Concha-Benavente, F., Gibson, S.P., Reeder, C., Ferrone, S., and Ferris, R.L. (2017). CD137 Stimulation Enhances Cetuximab-Induced Natural Killer: Dendritic Cell Priming of Antitumor T-Cell Immunity in Patients with Head and Neck Cancer. Clin. Cancer Res. *23*, 707–716. https://doi.org/10.1158/1078-0432.CCR-16-0879.
23. Pozzi, C., Cuomo, A., Spadoni, I., Magni, E., Silvola, A., Conte, A., Sigismund, S., Ravenda, P.S., Bonaldi, T., Zampino, M.G., et al. (2016). The EGFR-specific antibody cetuximab combined with chemotherapy triggers immunogenic cell death. Nat. Med. *22*, 624–631. https://doi.org/10.1038/nm.4078.
24. Vanneman, M., and Dranoff, G. (2012). Combining immunotherapy and targeted therapies in cancer treatment. Nat. Rev. Cancer *12*, 237–251. https://doi.org/10.1038/nrc3237.
25. Bourhis, J., Stein, A., Paul de Boer, J., Van Den Eynde, M., Gold, K.A., Stintzing, S., Becker, J.C., Moran, M., Schroeder, A., Pennock, G., et al. (2021). Avelumab and cetuximab as a therapeutic combination: An overview of scientific rationale and current clinical trials in cancer. Cancer Treat Rev. *97*, 102172. https://doi.org/10.1016/j.ctrv.2021.102172.
26. El Sissy, C., Kirilovsky, A., Van den Eynde, M., Mușină, A.M., Anitei, M.G., Romero, A., Marliot, F., Junca, A., Doyen, J., Mlecnik, B., et al. (2020). A Diagnostic Biopsy-Adapted Immunoscore Predicts Response to Neoadjuvant Treatment and Selects Patients with Rectal Cancer Eligible for a Watch-and-Wait Strategy. Clin. Cancer Res. *26*, 5198–5207. https://doi.org/10.1158/1078-0432.CCR-20-0337.
27. Barua, S., Fang, P., Sharma, A., Fujimoto, J., Wistuba, I., Rao, A.U.K., and Lin, S.H. (2018). Spatial interaction of tumor cells and regulatory T cells correlates with survival in non-small cell lung cancer. Lung Cancer *117*, 73–79. https://doi.org/10.1016/j.lungcan.2018.01.022.
28. Wang, E., Worschech, A., and Marincola, F.M. (2008). The immunologic constant of rejection. Trends Immunol. *29*, 256–262. https://doi.org/10.1016/j.it.2008.03.002.
29. Roelands, J., Kuppen, P.J.K., Ahmed, E.I., Mall, R., Masoodi, T., Singh, P., Monaco, G., Raynaud, C., de Miranda, N.F.C.C., Ferraro, L., et al. (2023). An integrated tumor, immune and microbiome atlas of colon cancer. Nat. Med. *29*, 1273–1286. https://doi.org/10.1038/s41591-023-02324-5.
30. Angelova, M., Mlecnik, B., Vasaturo, A., Bindea, G., Fredriksen, T., Lafontaine, L., Buttard, B., Morgand, E., Bruni, D., Jouret-Mourin, A., et al. (2018). Evolution of Metastases in Space and Time under Immune Selection. Cell *175*, 751–765.e16. https://doi.org/10.1016/j.cell.2018.09.018.
31. Mayer, R.J., Van Cutsem, E., Falcone, A., Yoshino, T., Garcia-Carbonero, R., Mizunuma, N., Yamazaki, K., Shimada, Y., Tabernero, J., Komatsu, Y., et al. (2015). Randomized trial of TAS-102 for refractory metastatic colorectal cancer. N. Engl. J. Med. *372*, 1909–1919. https://doi.org/10.1056/NEJMoa1414325.
32. Grothey, A., Van Cutsem, E., Sobrero, A., Siena, S., Falcone, A., Ychou, M., Humblet, Y., Bouché, O., Mineur, L., Barone, C., et al. (2013). Regorafenib monotherapy for previously treated metastatic colorectal cancer (CORRECT): an international, multicentre, randomised, placebo-controlled, phase 3 trial. Lancet *381*, 303–312. https://doi.org/10.1016/S0140-6736(12)61900-X.
33. Dasari, A., Lonardi, S., Garcia-Carbonero, R., Elez, E., Yoshino, T., Sobrero, A., Yao, J., García-Alfonso, P., Kocsis, J., Cubillo Gracian, A., et al. (2023). Fruquintinib versus placebo in patients with refractory metastatic colorectal cancer (FRESCO-2): an international, multicentre, randomised, double-blind, phase 3 study. Lancet *402*, 41–53. https://doi.org/10.1016/S0140-6736(23)00772-9.
34. Prager, G.W., Taieb, J., Fakih, M., Ciardiello, F., Van Cutsem, E., Elez, E., Cruz, F.M., Wyrwicz, L., Stroyakovskiy, D., Pápai, Z., et al. (2023). Trifluridine-Tipiracil and Bevacizumab in Refractory Metastatic Colorectal Cancer. N. Engl. J. Med. *388*, 1657–1667. https://doi.org/10.1056/NEJMoa2214963.
35. Le, D.T., Uram, J.N., Wang, H., Bartlett, B.R., Kemberling, H., Eyring, A.D., Skora, A.D., Luber, B.S., Azad, N.S., Laheru, D., et al. (2015). PD-1 Blockade in Tumors with Mismatch-Repair Deficiency. N. Engl. J. Med. *372*, 2509–2520. https://doi.org/10.1056/NEJMoa1500596.
36. Overman, M.J., Lonardi, S., Wong, K.Y.M., Lenz, H.J., Gelsomino, F., Aglietta, M., Morse, M.A., Van Cutsem, E., McDermott, R., Hill, A., et al. (2018). Durable Clinical Benefit With Nivolumab Plus Ipilimumab in DNA Mismatch Repair-Deficient/Microsatellite Instability-High Metastatic Colorectal Cancer. J. Clin. Oncol. *36*, 773–779. https://doi.org/10.1200/JCO.2017.76.9901.
37. Ganesh, K., Stadler, Z.K., Cercek, A., Mendelsohn, R.B., Shia, J., Segal, N.H., and Diaz, L.A., Jr. (2019). Immunotherapy in colorectal cancer: rationale, challenges and potential. Nat. Rev. Gastroenterol. Hepatol. *16*, 361–375. https://doi.org/10.1038/s41575-019-0126-x.
38. Van den Eynde, M., Mlecnik, B., Bindea, G., Fredriksen, T., Church, S.E., Lafontaine, L., Haicheur, N., Marliot, F., Angelova, M., Vasaturo, A., et al. (2018). The Link between the Multiverse of Immune Microenvironments in Metastases and the Survival of Colorectal Cancer Patients. Cancer Cell *34*, 1012–1026.e3. https://doi.org/10.1016/j.ccell.2018.11.003.
39. Ciardiello, D., Famiglietti, V., Napolitano, S., Esposito, L., Pietrantonio, F., Avallone, A., Maiello, E., Cremolini, C., Troiani, T., Martinelli, E., et al. (2022). Final results of the CAVE trial in RAS wild type metastatic colorectal cancer patients treated with cetuximab plus avelumab as rechallenge therapy: Neutrophil to lymphocyte ratio predicts survival. Clin. Colorectal Cancer *21*, 141–148. https://doi.org/10.1016/j.clcc.2022.01.005.

40. Napolitano, S., Martini, G., Ciardiello, D., Di Maio, M., Normanno, N., Avallone, A., Martinelli, E., Maiello, E., Troiani, T., and Ciardiello, F. (2022). CAVE-2 (Cetuximab-AVElumab) mCRC: A Phase II Randomized Clinical Study of the Combination of Avelumab Plus Cetuximab as a Rechallenge Strategy in Pre-Treated RAS/BRAF Wild-Type mCRC Patients. Front. Oncol. *12*, 940523. https://doi.org/10.3389/fonc.2022.940523.

41. Cremolini, C., Rossini, D., Dell'Aquila, E., Lonardi, S., Conca, E., Del Re, M., Busico, A., Pietrantonio, F., Danesi, R., Aprile, G., et al. (2019). Rechallenge for Patients With RAS and BRAF Wild-Type Metastatic Colorectal Cancer With Acquired Resistance to First-line Cetuximab and Irinotecan: A Phase 2 Single-Arm Clinical Trial. JAMA Oncol. *5*, 343–350. https://doi.org/10.1001/jamaoncol.2018.5080.

42. Martinelli, E., Martini, G., Famiglietti, V., Troiani, T., Napolitano, S., Pietrantonio, F., Ciardiello, D., Terminiello, M., Borrelli, C., Vitiello, P.P., et al. (2021). Cetuximab Rechallenge Plus Avelumab in Pretreated Patients With RAS Wild-type Metastatic Colorectal Cancer: The Phase 2 Single-Arm Clinical CAVE Trial. JAMA Oncol. *7*, 1529–1535. https://doi.org/10.1001/jamaoncol.2021.2915.

43. Sartore-Bianchi, A., Pietrantonio, F., Lonardi, S., Mussolin, B., Rua, F., Crisafulli, G., Bartolini, A., Fenocchio, E., Amatu, A., Manca, P., et al. (2022). Circulating tumor DNA to guide rechallenge with panitumumab in metastatic colorectal cancer: the phase 2 CHRONOS trial. Nat. Med. *28*, 1612–1618. https://doi.org/10.1038/s41591-022-01886-0.

44. Ciardiello, D., Martinelli, E., Troiani, T., Mauri, G., Rossini, D., Martini, G., Napolitano, S., Famiglietti, V., Del Tufo, S., Masi, G., et al. (2024). Anti-EGFR Rechallenge in Patients With Refractory ctDNA RAS/BRAF wt Metastatic Colorectal Cancer: A Nonrandomized Controlled Trial. JAMA Netw. Open *7*, e245635. https://doi.org/10.1001/jamanetworkopen.2024.5635.

45. Tougeron, D., Emile, J.F., Bodere, A., Barbier, E., Bez, J., Dourthe, L.M., Perrier, H., Corbinais, S., Le Brun-Ly, V., Bideau, K., et al. (2024). 502O Pembrolizumab in combination with CAPOX and bevacizumab in patients with microsatellite stable metastatic colorectal cancer and a high immune infiltrate: Preliminary results of FFCD 1703 POCHI trial. Ann. Oncol. *35*, S428. https://doi.org/10.1016/j.annonc.2024.08.571.

46. Nobin, H., Garvin, S., Hagman, H., Nodin, B., Jirström, K., and Brunnström, H. (2024). The prognostic value of programmed death-ligand 1 (PD-L1) expression in resected colorectal cancer without neoadjuvant therapy - differences between antibody clones and cell types. BMC Cancer *24*, 1051. https://doi.org/10.1186/s12885-024-12812-7.

47. Wang, X., Teng, F., Kong, L., and Yu, J. (2016). PD-L1 expression in human cancers and its association with clinical outcomes. OncoTargets Ther. *9*, 5023–5039. https://doi.org/10.2147/ott.s105862.

48. Overman, M.J., McDermott, R., Leach, J.L., Lonardi, S., Lenz, H.J., Morse, M.A., Desai, J., Hill, A., Axelson, M., Moss, R.A., et al. (2017). Nivolumab in patients with metastatic DNA mismatch repair-deficient or microsatellite instability-high colorectal cancer (CheckMate 142): an open-label, multicentre, phase 2 study. Lancet Oncol. *18*, 1182–1191. https://doi.org/10.1016/S1470-2045(17)30422-9.

49. Saberzadeh-Ardestani, B., Graham, R.P., McMahon, S., Ahanonu, E., Shi, Q., Williams, C., Hubbard, A., Zhang, W., Muranyi, A., Yan, D., et al. (2023). Immune Marker Spatial Distribution and Clinical Outcome after PD-1 Blockade in Mismatch Repair-deficient, Advanced Colorectal Carcinomas. Clin. Cancer Res. *29*, 4268–4277. https://doi.org/10.1158/1078-0432.CCR-23-1109.

50. Chalabi, M., Fanchi, L.F., Dijkstra, K.K., Van den Berg, J.G., Aalbers, A.G., Sikorska, K., Lopez-Yurda, M., Grootscholten, C., Beets, G.L., Snaebjornsson, P., et al. (2020). Neoadjuvant immunotherapy leads to pathological responses in MMR-proficient and MMR-deficient early-stage colon cancers. Nat. Med. *26*, 566–576. https://doi.org/10.1038/s41591-020-0805-8.

51. Ladoire, S., Martin, F., and Ghiringhelli, F. (2011). Prognostic role of FOXP3 + regulatory T cells infiltrating human carcinomas: the paradox of colorectal cancer. Cancer Immunol. Immunother. *60*, 909–918. https://doi.org/10.1007/s00262-011-1046-y.

52. Shang, B., Liu, Y., Jiang, S.J., and Liu, Y. (2015). Prognostic value of tumor-infiltrating FoxP3+ regulatory T cells in cancers: a systematic review and meta-analysis. Sci. Rep. *5*, 15179. https://doi.org/10.1038/srep15179.

53. Bindea, G., Mlecnik, B., Fridman, W.H., and Galon, J. (2011). The prognostic impact of anti-cancer immune response: a novel classification of cancer patients. Semin. Immunopathol. *33*, 335–340. https://doi.org/10.1007/s00281-011-0264-x.

54. Bindea, G., Mlecnik, B., Angell, H.K., and Galon, J. (2014). The immune landscape of human tumors: Implications for cancer immunotherapy. OncoImmunology *3*, e27456. https://doi.org/10.4161/onci.27456.

55. Church, S.E., and Galon, J. (2015). Tumor Microenvironment and Immunotherapy: The Whole Picture Is Better Than a Glimpse. Immunity (Camb., Mass.) *43*, 631–633. https://doi.org/10.1016/j.immuni.2015.10.004.

56. Marliot, F., Chen, X., Kirilovsky, A., Sbarrato, T., El Sissy, C., Batista, L., Van den Eynde, M., Haicheur-Adjouri, N., Anitei, M.G., Musina, A.M., et al. (2020). Analytical validation of the Immunoscore and its associated prognostic value in patients with colon cancer. J. Immunother. Cancer *8*, e000272. https://doi.org/10.1136/jitc-2019-000272.

57. Chomczynski, P., and Sacchi, N. (2006). The single-step method of RNA isolation by acid guanidinium thiocyanate-phenol-chloroform extraction: twenty-something years on. Nat. Protoc. *1*, 581–585. https://doi.org/10.1038/nprot.2006.83.

58. Huyghe, N., Benidovskaya, E., Beyaert, S., Daumerie, A., Maestre Osorio, F., Aboubakar Nana, F., Bouzin, C., and Van den Eynde, M. (2023). Multiplex Immunofluorescence Combined with Spatial Image Analysis for the Clinical and Biological Assessment of the Tumor Microenvironment. J. Vis. Exp. https://doi.org/10.3791/65220.

59. Dobin, A., Davis, C.A., Schlesinger, F., Drenkow, J., Zaleski, C., Jha, S., Batut, P., Chaisson, M., and Gingeras, T.R. (2013). STAR: ultrafast universal RNA-seq aligner. Bioinformatics *29*, 15–21. https://doi.org/10.1093/bioinformatics/bts635.

60. Li, H., Handsaker, B., Wysoker, A., Fennell, T., Ruan, J., Homer, N., Marth, G., Abecasis, G., and Durbin, R.; 1000 Genome Project Data Processing Subgroup (2009). The Sequence Alignment/Map format and SAMtools. Bioinformatics *25*, 2078–2079. https://doi.org/10.1093/bioinformatics/btp352.

61. Pertea, M., Pertea, G.M., Antonescu, C.M., Chang, T.C., Mendell, J.T., and Salzberg, S.L. (2015). StringTie enables improved reconstruction of a transcriptome from RNA-seq reads. Nat. Biotechnol. *33*, 290–295. https://doi.org/10.1038/nbt.3122.

62. Love, M.I., Huber, W., and Anders, S. (2014). Moderated estimation of fold change and dispersion for RNA-seq data with DESeq2. Genome Biol. *15*, 550. https://doi.org/10.1186/s13059-014-0550-8.

63. Jiménez-Sánchez, A., Cast, O., and Miller, M. (2018). Comprehensive Benchmarking and Integration of Tumour Microenvironment Cell Estimation Methods. Preprint at: bioRxiv, 437533. https://doi.org/10.1101/437533

64. Wilkerson, M.D., and Hayes, D.N. (2010). ConsensusClusterPlus: a class discovery tool with confidence assessments and item tracking. Bioinformatics *26*, 1572–1573. https://doi.org/10.1093/bioinformatics/btq170.

65. Szolek, A., Schubert, B., Mohr, C., Sturm, M., Feldhahn, M., and Kohlbacher, O. (2014). OptiType: precision HLA typing from next-generation sequencing data. Bioinformatics *30*, 3310–3316. https://doi.org/10.1093/bioinformatics/btu548.

66. Zhang, J., Caruso, F.P., Sa, J.K., Justesen, S., Nam, D.H., Sims, P., Ceccarelli, M., Lasorella, A., and Iavarone, A. (2019). The combination of neoantigen quality and T lymphocyte infiltrates identifies glioblastomas with the longest survival. Commun. Biol. *2*, 135. https://doi.org/10.1038/s42003-019-0369-7.

STAR★METHODS

KEY RESOURCES TABLE

REAGENT or RESOURCE	SOURCE	IDENTIFIER
Antibodies		
Monoclonal anti-PD-L1(avelumab)	Merck KGaA	BAVENCIO
Monoclonal anti-EGFR (cetuximab)	Merck KGaA	Erbitux
Rabbit monoclonal anti-CD3 ε antibody (IF)	Abcam	# ab16669, clone SP7; RRID:AB_443425
Mouse monoclonal anti-CD8 (IF)	Agilent	# M7103, clone C8/144B; RRID:AB_2075537,
Mouse monoclonal anti-PD-1 (IF)	Abcam	# ab52587, clone NAT105; RRID:AB_881954
Rabbit monoclonal anti-PD-L1 (IF)	Cell Signaling	# 13684, clone E1L3N; RRID:AB_2687655
Mouse monoclonal anti-CD45RO (IF)	Cell Signaling	# 55618, clone UCHL1; RRID:AB_2799491
Mouse monoclonal anti-FOXP3 (IF)	Abcam	# ab20034, clone 236A/E7; RRID:AB_445284
Rabbit monoclonal anti-SMAD3 (pS423/425)	Abcam	# ab52903, clone EP823Y; RRID:AB_882596
Rabbit monoclonal anti-Galectin-9 (IF)	Cell Signaling	# 54330, clone D9R4A; RRID:AB_2799456
Mouse monoclonal anti-Cytokeratin (IF)	Agilent	# M3515, clone AE1/AE3; RRID:AB_2132885
Mouse monoclonal anti-CD68 (IF)	Agilent	# GA613, clone PG-M1; RRID:AB_2074844
Rabbit monoclonal anti-NCR1 (NKP46) (IF)	Abcam	# ab224703, clone EPR22403-57; RRID:AB_3096083
Mouse monoclonal anti-HLA class I ABC (IF)	Abcam	# ab70328, clone EMR8-5; RRID:AB_1269092
Biological samples		
Liver/lung metastases biopsies of mCRC	Cliniques Universitaires St-Luc, Belgium	NCT03608046
Liver/lung metastases biopsies of mCRC	Grand Hôpital de Charleroi, Belgium	NCT03608046
Chemicals, peptides, and recombinant proteins		
Irinotecan	Accord	Irinotecan Accord
Guanidine isothiocyanate	Fluka	# 50990
Cesium Chloride	BRL	# 540-5507 UB
RNAlater Stabilization Solution	Invitrogen/ThermoFischer scientific	# AM7023
EnVision+ System- HRP Labelled Polymer Anti-Rabbit	Agilent	# K4003
EnVision+ System- HRP Labelled Polymer Anti-Mouse	Agilent	# K4001
Alexa Fluor™ 488	ThermoFischer Scientific	# B40953
Alexa Fluor™ 555	ThermoFischer Scientific	# B40955
Alexa Fluor™ 594	ThermoFischer Scientific	# B40957
Alexa Fluor™ 647	ThermoFischer Scientific	# B40958
Tyramide-CF754	Biotium	# 96090
Hoechst 33342, trihydrochloride trihydrate, 10 mg/mL solution in water	ThermoFischer Scientific	# H3570
Fluorescence mounting medium	DAKO	# S3023
Bovine Serum Albumin	Sigma	# A9418-50G
Pierce™ DAB Substrate Kit	ThermoFischer Scientific	# 34002
Paraformaldehyde Solution, 4%	ThermoFischer Scientific	# J19943.K2
Dewax Solution	Leica	# AR9222
Bond TM Epitope Retrieval 1	Leica	# AR9961
Bond TM Epitope Retrieval 2	Leica	# AR9640

(*Continued on next page*)

Continued

REAGENT or RESOURCE	SOURCE	IDENTIFIER
Critical commercial assays		
RNeasy Mini Kit	Qiagen	# 74104
NucleoSpin Tissue, Mini kit for DNA from cells and tissue	Macherey Nagel	# 740952
RNA 6000 Nano Kit	Agilent	# 5067-1511
PAXgene Blood DNA Kit	Qiagen	# 20020595
Superscript IV Reverse Transcriptase	ThermoFischer Scientific	# 18090010
SureSelect XT Low Input enrichment kit	Agilent	# G9707B
Herculase II fusion DNA polymerase	Agilent	# 600675
Quant-iT broad range dsDNA Assay	ThermoFischer Scientific	# Q33130
Deposited data		
Processed, anonymized summary data	This study	Mendeley Data: https://doi.org/10.17632/ffb35993tw.1
Anonymized gene count matrix	This study	Mendeley Data: https://doi.org/10.17632/ffb35993tw.1
Anonymized VCF files	This study	Mendeley Data: https://doi.org/10.17632/ffb35993tw.1
Anonymized MAF files	This study	Mendeley Data: https://doi.org/10.17632/ffb35993tw.1
Software and algorithms		
GRCh38 genome assembly	ENSEMBL	http://www.ensembl.org/Homo_sapiens/Info/Index
R (v 4.4.2)	The R Project for Statistical Computing	http://www.r-project.org/
R scripts and codes	This study	Mendeley Data: https://doi.org/10.17632/ffb35993tw.1
HALO (v3.3) | Quantitative Image Analysis for Pathology	Indica labs	HALO | Quantitative Image Analysis for Pathology - Indica Labs
FastQC	s-andrews	https://github.com/s-andrews/FastQC
STAR	Alexdobin	https://github.com/alexdobin/STAR
Samtools	Samtools	https://www.htslib.org/
Stringtie	gpertea	https://github.com/gpertea/stringtie
Other		
gentleMACS^{TM} Octo Dissociator	Miltenyi Biotec	# 130-096-427
Optima LE-80K Ultracentrifuge	Beckman Coulter	N/A
SW-60 Ti swinging bucket rotors	Beckman Coulter	# 335649
Agilent 2100 Bioanalyser	Agilent	# 761115
LabChip GXII Touch HT	PerkinElmer	N/A
BOND RXm Fully Automated IHC/ISH Research Stainer	Leica Biosystems	# 21.2821
PAXgene Blood DNA Tubes	QIAGEN	# 761115
4 mL, Open-Top Thinwall Ultra-Clear Tube	Beckman Coulter	# 344062
Axioscan Z1	Zeiss	N/A
Borosilicate Cover Glass	VWR	# 631-0146

EXPERIMENTAL MODEL AND SUBJECT DETAILS

Study design and participants

The AVETUXIRI trial (NCT03608046) was conducted as a multi-center, open-label, phase 2 non-randomized proof of concept study. The trial was initiated on 03/08/2018 and concluded on 21/02/2023. Fifty-seven patients were prospectively enrolled at the Cliniques universitaires St-Luc (CUSL) and Grand Hôpital de Charleroi (GHdC), and 55 started the study treatment. Patient were allocated to cohort A (*RAS*-WT tumor) or cohort B and C (*RAS*-MUT) overtime. The analysis was based on intent-to-treat (ITT) and Evaluable Patients Population (EPP) comprising all patients (cohorts A, B, and C) who were included and received at least one cycle of the study treatment (1 complete infusion of avelumab and Irinotecan and 2 complete infusions of cetuximab). Efficacy results from EPP are presented in this manuscript and used for exploratory analyses.

The major eligibility criteria included: metastatic CRC adenocarcinoma; pMMR, as proven by immunohistochemistry (IHC) for mismatch repair proteins (MLH1, MSH2, MSH6, PMS2), or MSS determined by PCR for microsatellite instability markers; *BRAFV600E* wild-type; refractory to standard chemotherapy (fluoropyrimidine, oxaliplatin, irinotecan) and anti-EGFR treatment (only for *RAS*-WT tumor); a measurable disease (RECIST 1.1) with at least one metastasis accessible for sequential biopsies; aged ≥18 years old; an Eastern Cooperative Oncology Group performance status 0–1; an adequate organ function and life expectancy of at least 4 months. The exclusion criteria mainly comprised of active autoimmune diseases, administration of immunosuppressive medication, past exposure to immunotherapy, regorafenib, trifluridine/tipiracil and non-progressive disease following irinotecan-based treatment and anti-EGFR treatment (for *RAS*-WT tumor only). The full inclusion and exclusion criteria are provided in the protocol (supp material).

All participants provided written informed consent. The trial protocol and amendments were approved by the ethical committee of CUSL and GHdC. This trial was conducted in full conformance with the ICH E6 guideline for Good Clinical Practice (GCP) and the principles of the Declaration of Helsinki.

METHOD DETAILS

Procedures

Included patients (all cohorts) received cetuximab (400 mg/m2 loading dose week 1, 250 mg/m2 at week 2 followed by 500 mg/m2 from week 3) and irinotecan (150 mg/m2/2 weeks) from week 1. Avelumab (10 mg/kg/2 weeks) started from week 3 (concomitantly the day of the third injection of cetuximab and second injection of irinotecan). A first disease assessment (iRECIST 1.1) was performed at week 11 (8 weeks after starting avelumab) and thereafter every 8 weeks. Adverse events were monitored throughout treatment and for 90 days after the last dose of treatment. Safety analyses were performed using the Common Terminology Criteria for Adverse Events (CTCAE), version 4.03.

Sequential metastases biopsies (liver or other accessible CRC metastasis) were performed over time: at baseline before treatment start (week 0), before the first injection of avelumab (week 3) and at the first disease assessment (during week 11). All patients enrolled in the study consented for metastasis biopsies.

Outcomes and statistical considerations

Primary endpoints for cohorts A and B were (i) overall tumor response rate (ORR) defined the proportion of all included patients with a confirmed partial or complete response and (ii) safety measured by the frequency and grade of adverse events using CTCAEv4.03. Primary endpoint of cohort C were 6 months PFS-rate (proportion of patients without progression 6 months after trial inclusion) and safety. Secondary endpoints comprised duration of response, disease control rate, PFS and OS. Exploratory objectives planned an in-depth investigation of the immunological features of the tumor and its surrounding microenvironment (including Immunoscore biomarkers) to discover predictive biomarkers of efficacy.

The sample size was based on a Simon Optimum two-stage design in cohort of RAS-WT (cohort A) and RAS-MUT (cohorts B and cohort C) chemo refractory mCRC patients.

Based on a Simon 2-stage design ($\alpha = 0.1$; $\beta = 0.2$) for ORR (cohorts A: P0/P1 = 0.15/0.33 – B: P0/P1 = 0.09/0.25) and 6 months PFS rate (cohort C: P0/P1 = 0.15/0.31), 10 + 18 (cohort A: stage 1+stage 2); 13 + 15 (cohort B) and 14 + 25 (cohort C) patients were required. At least 2 + 5 (cohort A: stage 1+stage 2); 2 + 3 (cohort B) and 3 + 6 (cohort C) patients were to reach ORR (cohorts A-B) or 6 months PFS rate (cohort C) for efficacy objectives.

For exploratory analyses, cohort B and C (similar treatment procedure) were pooled to report results for RAS-MUT cohorts.

Sample processing

For each patient, two adjacent metastatic tumor biopsy samples were obtained at baseline (week 0), week 3, and week 11 (Figure 1). One biopsy was preserved in RNALater for subsequent RNA and DNA extraction. Total RNA and DNA were isolated using guanidine isothiocyanate (GITC) method.[57] Biopsies were lysed in 4 M GITC followed by homogenization with a gentleMACS™ Octo Dissociator and a 22-G needle to ensure uniformity. Ultracentrifugation in a 5.7 M Cesium Chloride CsCl gradient (GITC/CsCl: 3/1) was performed with SW-60 swinging bucket rotors at 41,000 rpm for 16 h to separate RNA, DNA, and protein fractions. RNA pellets from the GITC phase were purified using the RNeasy Mini Kit, involving membrane washing, elution, and DNase treatment to remove residual DNA. DNA was further purified from the CsCl phase with the NucleoSpin Tissue kit, including ethanol precipitation, silica column binding, and elution in a pre-warmed buffer. RNA and DNA concentrations and purity were assessed using a Nanodrop spectrophotometer, and RNA integrity was evaluated with the Agilent RNA 6000 Nano Kit, with samples having an RNA Integrity Number (RIN) above 7 selected for further analysis. The second biopsy was immediately fixed in 4% paraformaldehyde and embedded in paraffin (FFPE) for immunofluorescence staining. Additionally, blood samples were collected in PAXgene Blood DNA Tubes for germline DNA extraction using the PAXgene Blood DNA Kit.

Multiplex immunofluorescence

Hematoxylin and eosin staining

All FFPE biopsies were analyzed following staining with hematoxylin and eosin. Biopsies without tumor cells (containing only healthy liver or lung tissue), as well as those with dominant necrosis or fibrosis containing extremely low number of tumor cells (<3-5%) were excluded for mIF staining analyses. Biopsies were not excluded based on size.

Antigen staining

Five μm tissue sections were cut and mounted on Leica BOND slides, then dried overnight at room temperature. Multiplex immunofluorescence (mIF) staining was performed using a Leica BOND RXm autostainer with three panels of antigens developed and optimized as previously described.[58] Panel 1 included CD3 (1/100, pH6), CD8 (1/200, pH6), PD-1 (1/50, pH6), PD-L1 (1/1000, pH9), and CD45-RO (1/100, pH6); Panel 2 included CD3 (1/100, pH6), FOXP3 (1/500, pH6), pSMAD3 (1/100, pH9), and GAL-9 (1/800, pH6); Panel 3 included CD3 (1/100, pH6), hPan-CK (1/50, pH6), CD68 (1/500, pH6), NKP46 (1/500, pH6), and HLA class I A-B-C (1/200, pH6). The presence of PD-L1 was confirmed by immunochemistry using DAB (3,3′-diaminobenzidine) substrate.

Sections were initially deparaffinized with the Leica BOND dewax solution and protocol, then treated with 3% hydrogen peroxide in isopropanol for 10 min to inhibit endogenous peroxidases. After rinsing with distilled TBS-Tween 20 (TBS-T), tyramide signal amplification (TSA) staining was performed sequentially for each antigen.

Epitope retrieval was conducted on the Leica BOND system using either BOND epitope retrieval solution 1 (pH 6) or 2 (pH 9), depending on the specific antigen. Buffers were heated to 100°C, then cooled for 15 min and rinsed in TBS-T three times.

For blocking, sections were incubated with 5% bovine serum albumin (BSA) in TBS-T for 30 min. After the blocking solution was removed, sections were incubated with primary antibodies diluted in 1% BSA TBS-T for 60 min, followed by three 3-min TBS-T washes. Sections were then incubated with a secondary antibody (DAKO EnVision+ poly-HRP, anti-mouse or anti-rabbit) for 40 min, followed by an additional three 3-min TBS-T washes.

For TSA, sections were incubated with Alexa Fluor (ThermoFisher) tyramide reagent (diluted 1:200 in borate buffer, 0.1 M, pH 7.8, 3M NaCl, supplemented with 0.003% H_2O_2) for 15 min. This TSA staining sequence, including epitope retrieval and TSA incubation, was repeated for each antigen.

After TSA staining, nuclei were counterstained with a 20 mM Hoechst 33342 solution (diluted 1:1000 in 10% BSA TBS-T) for 5 min, followed by three rinses in distilled water. Sections were then manually mounted with Dako Fluorescence Mounting Medium and covered with VWR borosilicate cover glasses for imaging.

Slide scanning and image analysis

After multiplex staining, slides were digitized in fluorescence using a Zeiss Axioscan.z1 slide scanner at 20x magnification with custom filter sets. For image analysis, HALO software (v3.3, Indica Labs) with the HighPlex fluorescence module was used. Stromal and tumor nuclei were detected using the DenseNet AI V.2 plugin, which was pre-trained on Hoechst-stained nuclei across slides from multiple batches. After nuclei detection, fluorescence thresholds were calibrated for membrane and nuclear staining in each channel, with a percentage of completeness parameter set to minimize false positives in cases where adjacent cells displayed different staining patterns. Following these parameter adjustments, tumoral regions in biopsy samples were analyzed, and a data table for each biopsy was generated, containing positional coordinates (Xmin, Xmax; Ymin, Ymax) and marker positivity for each cell.

ISb, ISb_20 and heatmap

Following image analysis, data tables for each biopsy corresponding to the three mIF panels were imported into R (v4.4.2). The surface area of each biopsy was calculated using the concaveman package (v1.1.0), and the density of each marker combination was computed. The G-cross function from the spatstat package (v1.64) was used to estimate the distribution of distances from specific cell types to the nearest tumor cell. The area under the curve (AUC) at 20 μm was then calculated using the AUC function from the DescTools package (v0.99.58).

To compute the biopsy-adapted Immunoscore (ISb), we followed a previously described method.[26] Briefly, the densities of $CD3^+$ and $CD8^+$ cells were transformed into percentiles using the percent_rank function from dplyr (v1.4.4), and the mean percentiles of $CD3^+$ and $CD8^+$ cells were computed. Biopsies with a mean percentile below 25% were classified as ISb-Low, those between 25% and 70% as ISb-Medium, and those above 70% as ISb-High.

To compute the distance-based biopsy-adapted Immunoscore (ISb_20), the same methodology was applied, using the AUC value of the G-cross function at 20 μm for $CD3^+$ and $CD8^+$ cells instead of the density.

Heatmaps of density and distance values were generated using the ComplexHeatmap package (v3.20), where density and AUC values were transformed into Z-scores by scaling and centering the respective matrices with the scale function in base R. Unsupervised clustering was performed using the Euclidean distance method.

Gene expression

RNA-sequencing

The integrity and concentration of extracted RNA were assessed using the LabChip GXII Touch HT with RNA and DNA 5K/RNA/Charge Variant LabChip assays (PerkinElmer). mRNA libraries were constructed from 500 ng of total RNA using the Illumina TruSeq Stranded mRNA kit. For cDNA synthesis, Superscript IV Reverse Transcriptase (Thermo Fisher) was used, followed by 15 cycles of amplification after ligation with TruSeq RNA Combinatorial Dual-Index adapters. Clonal amplification and cluster generation were performed on the Illumina cBot 2 System. Sequencing was conducted on Illumina HiSeq platforms with 75 bp paired-end reads for 93% of samples and 150 bp reads for the remaining 7%, processed at the Clinical Genomics Laboratory, Sidra Medicine. The target read depth per sample was 20 million reads, with a mean achieved coverage of 18.4 million reads (SD 4.7 million).

Gene expression quantification and preprocessing

The raw sequencing data was processed and demultiplexed using the bcl2fastq2 tool. Quality control checks on the raw sequencing data were conducted using FastQC. Raw fastq files (R1 and R2) QC passed samples were aligned to the human reference genome

GRCh38 using the STAR RNA-seq aligner[59] along with the corresponding GTF file. Post alignment, quality control was carried out to assess the alignment quality and the overlap of paired-end mappings. The resulting alignment files (.bam) were processed with SAMtools,[60] and transcript abundances were estimated using Stringtie, an RNA-Seq data assembler.[61]

Differential expression analysis and gene set enrichment analysis

Pre-filtering to keep only rows that have a count of at least 10 for a minimal number of observations determined by the smallest group size was performed. Differential expression analysis was performed on raw gene-count matrix using R package DESeq 2.[62] Log2 Fold change of 1 and adjusted *p*-value of <0.05 was considered significant. R package ''ComplexHeatmap'' was used to visualize the top differentially expressed genes ($p < 0.01$) and Euclidean unsupervised method was used to determine clusters.

The gene list ranked by decreasing stat value was used for gene set enrichment analysis (GSEA) performed using R package ''clusterprofiler'' and MSigDB HALLMARK gene lists or GO terms. R package ''enrichplot'' and ''ggplot 2'' were used for pathway visualization.

Consensus TME analysis

Consensus tumor microenvironment cell estimation (ConsensusTME)[63] was performed to estimate relative abundancies of specific immune cell subsets from bulk transcriptome data. This method relies on integrated gene sets from multiple sources that have been curated and validated on a per-cancer-type basis, using benchmark datasets. It seems to outperform previously published methods. We applied ConsensusTME using R package ConsensusTME (v.0.0.1.9) using parameters ''COAD'' to specify cancer type and ''GSVA'' as statistical method.

ICR score

Consensus clustering was performed on a normalized log2-transformed expression matrix using 20 preselected ICR genes (*IFNG*, *IRF1*, *STAT1*, *IL12B*, *TBX21*, *CD8A*, *CD8B*, *CXCL9*, *CXCL10*, *CCL5*, *GZMB*, *GNLY*, *PRF1*, *GZMH*, *GZMA*, *CD274/PDL1*, *PDCD1*, *CTLA4*, *FOXP3*, *and IDO1*) (REF). The analysis utilized the R package ConsensusClusterPlus (v1.42.0)[64] with 5,000 iterations, employing agglomerative hierarchical clustering with Ward's method for inner linkage and complete linkage for outer clustering. The optimal number of clusters, determined using the Calinski–Harabasz criterion, was three. Tissue samples in the cluster with median or higher ICR gene expression were classified as 'ICR high,' while those below the median were designated as 'ICR low.' The average $\log_2$-transformed expression of the 20 ICR genes was defined as the ICR score.

Whole exome sequencing

DNA-sequencing

The library construction and sequencing was conducted at the Sidra Clinical Genomics Laboratory Sequencing Facility. To ensure the integrity of samples, we used the Genomic DNA assay on the Caliper Labchip GXII (PerkinElmer). DNA concentrations were quantified using the Quant-iT broad range dsDNA Assay (Thermo Fisher) on the FlexStation 3 Microplate reader (Molecular Devices). Whole Exome libraries were generated using the Agilent SureSelect XT Low Input enrichment kit, starting with 200 ng of input DNA. Enzymatic fragmentation of the DNA was carried out using the SureSelect Enzymatic Fragmentation Kit, targeting a fragment size of 250 bp. Library construction involved the use of Illumina-compatible adapters and single indices, followed by 8 cycles of amplification. To capture the exonic DNA, the Agilent SureSelectXT Human All Exon V6r2 capture library, covering 60 Mb of exonic regions, was utilized. The library was then incubated with biotinylated cRNA baits for 2 h, and the targeted regions were selected using magnetic streptavidin-coupled dynabeads. The amplified DNA was further processed using Agilent's Herculase II fusion DNA polymerase. Library quality was assessed using the DNA High Sensitivity Assay on a PerkinElmer Caliper GX2. Library quantification was performed using the KAPA HiFi Library quantification kit on a Roche LightCycler 480. Cluster generation was carried out on a cBot 1.0 or 2.0 using the HiSeq 3000/4000 PE Cluster Kit, followed by sequencing on an HiSeq 4000 instrument. The aim was to achieve a target coverage of 200X per sample, with flow cells loaded at a cluster density ranging from 1310 to 1524 K/mm2.

Sequence alignments and variant calling

BWA (v.0.7.12) was used to align the reads to the reference genome GRCh38/hg38. In the whole-exome sequencing (WES) analysis, the tumor and germline samples were sequenced with a 200X coverage. The median average coverage for tumor samples across all samples was 200X, with an interquartile range of 18, while it was 190X with an interquartile range of 10 for the germline samples. With respect to targeted exon coverage, more than 99% of the exons in tumor samples had coverage of at least 20-fold, and a minimum of 81% achieved a coverage over 70-fold. Trimadap (v.0.1.3) was used for adaptor trimming to eliminate adaptors from the sequencing reads. NGSCheckMate (v1.0.1) and ConPair analysis was done to estimate potential contamination and assess the agreement between paired normal and tumor samples. No mismatches were found in the samples, but potential contamination was indicated in two pairs. The results were confirmed using HLA typing data. All samples with contamination issues and identified mismatches were removed, leaving a final group of 108 biopsies for the final data analysis.

Somatic mutation calling and small insertions and deletions

SNVs were called using mutect (v.1.1.7) and somatic small insertions and deletions (indels) using strelka2 (bcbio-nextgen v.1.1.1). An optimized variant filtering pipeline was implemented to eliminate false-positive single-nucleotide variant calls. FiNGS (v1.7.2) was utilized with default settings, except for the following adjustments: minaltcount was set to 5, zeroproportion to 0.1, minmapquality-difference to 15, maxvafnormal to 0.2, and foxog to 0.99. MAF files were generated using the VCFtoMAF tool (v1.6.16), which included annotations for SIFT (Sorting Intolerant From Tolerant), PolyPhen, and the Exome Aggregation Consortium (ExAC). Variants observed in more than 1% of the general population, based on ExAC data, were filtered out. Following these technical exclusions,

biological filters were applied to select nonsynonymous mutations, including frameshift deletions, frameshift insertions, inframe deletions, inframe insertions, missense mutations, nonsense mutations, nonstop mutations, splice site mutations, and translation start site mutations. The resulting count of nonsynonymous variants/mutations per megabase (based on a capture size of 40 Mb) per sample was referred to as the nonsynonymous tumor mutational burden (TMB).

To visualize the most common somatic mutations and frequently altered pathways, the oncoplot function from the R package "maftools" (v2.1.2) was used with the parameter pathways = "sigpw". The TMB of the cohort was compared with the 33 TCGA cohorts using the tcgaCompare function, with a capture size of 38.5 Mb.

HLA typing, neoantigen prediction and GIE

HLA typing was conducted using OptiType (bcbio-nextgen v1.1.5 in Python v2.7.0)[65] on both WES and RNA-seq data. Neoantigen prediction was performed with the pVACseq tool from pVACtools, incorporating the following prediction algorithms: MHCnuggetsI, NNalign, NetMHC, SMM, SMMPMBEC, and SMMalign. The VCF files generated from the somatic mutation calling pipeline were used as input for pVACseq, along with HLA typing results obtained from WES data. Gene expression data aligned to GRCh38, measured in transcripts per million, was annotated to the VCFs using the vcf-expression-annotator. Mutant-specific binders associated with the relevant restricted HLA-I alleles were identified as neoantigens, following the criteria outlined by Zhang et al.[66] Neoantigens were defined as mutated epitopes with a median IC_{50} binding affinity <500 nM across all prediction algorithms, paired with corresponding wild-type epitopes showing a median IC_{50} binding affinity >500 nM. Predicted neoantigens were utilized to calculate the GIE (Global Immunoediting) value, which was determined as the ratio of observed to expected neoantigens. The expected neoantigen count was derived based on the assumption of a linear relationship between TMB and neoantigen number. Samples with fewer neoantigens than expected (lower GIE values) were interpreted as exhibiting evidence of immunoediting, while those with higher-than-expected neoantigen counts suggested a lack of immunoediting.

IES classification and analysis

The IES (Immune Environment Score) is a composite metric incorporating both ICR and GIE. Tumors classified as IES4 are predicted to have the highest immune activity, characterized by being ICR high and exhibiting GIE.[29] In contrast, IES1 tumors are considered the most immune-silent, being both ICR low and lacking GIE. The intermediate categories, IES2 and IES3, represent tumors that are ICR low but exhibit GIE and those that are ICR high but lack GIE, respectively.

QUANTIFICATION AND STATISTICAL ANALYSIS

Genetic immunoediting value

The GIE value is determined by calculating the ratio of the observed (O) to the expected (E) number of neoantigens:

$$\text{GIE value} = O/E$$

where E is a function of the number of nonsynonymous mutations in that specific sample (X)

$$E(x) = -2.38770 + 0.09171 \times X$$

G-cross function

Mathematically, the G-cross function is expressed as follows:

$$G_{xy}(r) = 1 - e^{-\lambda y \pi r 2}$$

The subscripts 'x' and 'y' specify that we are calculating the spatial distribution of cells of type 'y' in relation to cells of type 'x'. The term λy represents the overall density of 'y' cells within the slide. The area under the G-cross function curve reflects the extent of 'y' cell infiltration within a specified distance from 'x' cells.

Statistics

The Whitney–Wilcoxon rank-sum, and Fisher exact test were used for correlation analysis. Log rank test and cox proportional hazard was used for survival analysis. All statistical analyses were performed on R V4.4.2.

The study data were analyzed using SAS software (version 9.4; SAS Institute Inc, Cary, NC, USA) and R software (version 4.3.2). Figures were created with ggplot2 (v3.5.0), ggpubr (v0.6.0) and combined with patchwork (v1.2.0). Survival plots were created with survminer (v0.4.9) and survival (v3.5-8). Alluvial plots were created with ggalluvial (v0.12.5). Heatmaps were generated using the ComplexHeatmap package (v2.18.0).

ADDITIONAL RESOURCES

This work is part of the clinical trial AVETUXIRI, registered at ClinicalTrials.gov under the registry number NCT03608046.